Adaptive High Linearity Intensity Modulator for Advanced Microwave Photonic Links

Benjamin Dingel, Nicholas Madamopoulos and
Andru Prescod

Additional information is available at the end of the chapter

http://dx.doi.org/10.5772/intechopen.69262

Abstract

This chapter, first, presents the motivation behind the need for adaptive, highly linear electro-optic modulators and an overview of the different optical linearization approaches of electro-optic modulators. Then, the figures of merits in terms of linearity performance are described and analyzed. Next, the chapter focuses on one excellent linearization approach called interferometric modulator with phase-modulating and cavity-modulating components (IMPACC). Here, we model IMPACC by simulating each of the key building blocks separately before putting them together as IMPACC modulator. This adaptive IMPACC design is compared to typical Mach-Zehnder interferometer (MZI) based modulators, and ring-assisted Mach-Zenhder interferometer (RAMZI) modulators. Theoretical analysis and results show that the IMPACC provides both superior linearity performance and unique adaptive feature that can be used to compensate for manufacturing tolerances, thus, providing extra flexibility in terms of device manufacturability as well as system integration.

Keywords: linear optical intensity modulator, spurious free dynamic range, bandwidth, Mach Zehnder interferometer (MZI) modulator, resonator-assisted Mach Zehnder interferometer (RAMZI), interferometric modulator with phase-modulating and cavity-modulating components (IMPACC), broadband communication

1. Introduction

1.1. Technology trends in microwave photonic links (MPLs)

The current state of microwave photonic links (MPLs) is in the midst of transformation toward more dynamic and flexible MPLs, in response to three major on-going technical shifts, as depicted in **Figure 1**. The first technical shift is an outgrowth of the concept of *software-defined*

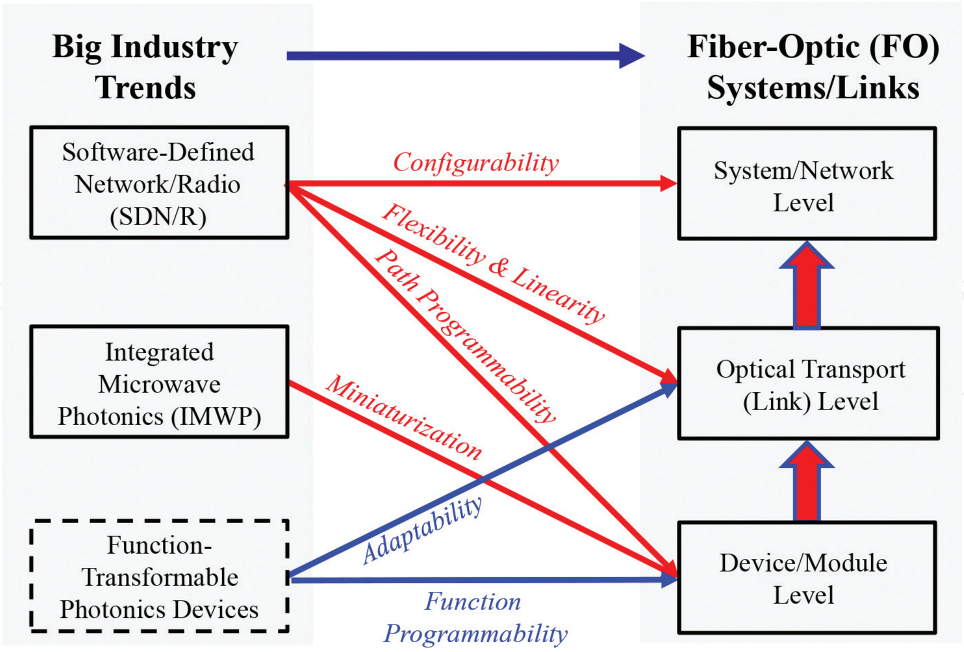

Figure 1. Technology shifts with SDN, integrated microwave photonic (IMWP) and function-transformable photonic devices are generating changes in the architecture, transport and module levels in the traditional fiber-optic links and systems.

networks (SDN) or software-defined radio (SDR) [1–6]. SDN/SDR is going to be investigated, demonstrated, and applied by the microwave photonics community from many different fronts. These include (i) architecture level for future networking needs, (ii) link level to support flexible optical transport layer needs, and even (iii) module level that requires programmable functions that are accessible by direct software control. This shift is driven further by ever expanding applications of MPLs in various "bandwidth-hungry" communication fields like cellular [7] and optical wireless [8], besides the traditional applications of cable television (CATV) [9], subcarrier multiplexing (SCM) optical communication systems [10–12], defense and military [13–16]. The overall goal is toward some form of *software-defined MPLs*.

Figure 2 shows one potential MPL in the context of a bigger configuration defined by SDN—a generic analog optical link, which we will refer to as SD-MPL. It consists of (i) a reconfigurable intensity-modulated direct-detection (IM-DD) link architecture, (ii) control plane, and (iii) network controller. The reconfigurable IM-DD comprises of three modules, namely (1) tunable transmitter, (2) fiber, and (3) receiver. The transmitter module consists of a tunable CW laser source, intensity modulator, RF driver, and RF amplifier, whereas the receiver module could be made up of fiber amplifier and photodetectors for a simple case, and might include DSP module with analog-to-digital converter (ADC) for a more sophisticated/advanced case.

Within the context of SDN, the control plane assembles, enables, and coordinates all pertinent control signals coming from and through the transmitter and receiver modules. Then, the network controller accesses the control plane through OpenFlow interface [5, 17–20] to configure the transmitter and receiver modules. For this generic architecture to function back to traditional, standalone MPLs, the network controller and control plane can be removed and

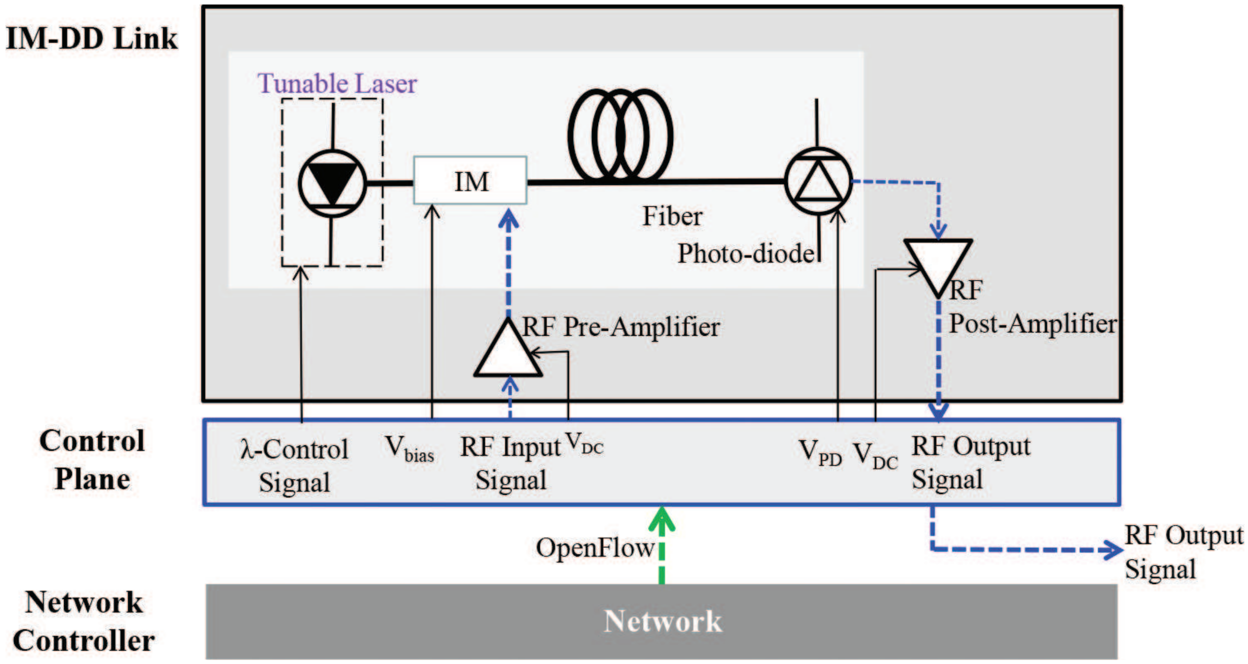

Figure 2. A generic software defined IM-DD-based MPLs in context of a bigger configuration defined by SDN.

the individual control signals are now transferred to the transmitter and receiver modules of the MPLs.

The second technical shift is the rapid growth of the field *integrated microwave photonics (IMWP)* [21–23], which used to be a niche research area some three decades ago. Today, *IMWP* aims to *miniaturize key photonic components, which are essential in the MPLs*, by using the emerging photonic integrated circuits (PICs) [23–26] technology to the level that would be comparable to the performance of state-of-the-art microwave components and systems [21]. Clearly, the rapid developments and advances [22, 23–26] in fabrication technologies re-enforce more advanced IMWP devices and support the prospect of future *software-defined* MPLs.

1.2. Device programmability

The third technical shift is happening at the module level with the development of optical programmable devices and components. These programmable devices and components can have the traditional features of reconfigurability, tunability, or selectability. There are growing number of reports and demonstrations of so-called *microwave photonics processors* [27–33].

Another implementation of these devices is based on the concept of a photonic field-programmable gate array (**FPGA**) or “Photonics FPGA”. It is the analogous version of the electronic **FPGA**, which is an integrated circuit designed to be configured by a customer or a designer after manufacturing. “Photonic FPGA” is geared toward arbitrary function generation or function programmability in miniaturized form, which is essential in the full implementation of SDN. This technology is still in the early stages of development, but the growing numbers of demonstrations of on-chip optical processing have been reported and they look promising [27–40].

1.3. Linearity

However, to really support the march toward future IMWP-assisted, software-defined MPLs, it is imperative that these new photonic components not only have inherent *programmable features* that can be accessed by software control, but also *superior linearity characteristics*. Note that microwave photonic links, in its basic form, is essentially a linearization engineering challenge. Regardless of whether we are talking about current MPLs or the future SD-MPLs, the core requirement of the links is still the same—high linearity links! *Superior device's linearity* translates to *high* overall link *performance*. The combination of superior linearity and programmability features in key photonics devices would lead to adaptive, highly linearity SD-MPLs.

1.4. Intensity-modulated direct detection (IM-DD) link and figure of merits

One of the most dominant optical transport schemes in MPLs is the intensity modulated direct detection (IM-DD) because of its simplicity and low cost. IM-DD scheme is shown in the upper portion of **Figure 2**. In its basic form, it consists of a RF data signal, laser source (either in the form of (i) directly modulated laser or (ii) externally modulated laser, using a combination of CW laser transmitter and optical modulator), optical fibers, optical and electrical amplifiers, and photodetector.

For most low-bandwidth (<1 GHz) applications, the directly modulated laser is used as a laser source for economic reason. However, for applications that require higher linearity, larger link gain and wider bandwidth (e.g., 1–60 GHz), the use of an externally modulated laser is the most viable and common approach. It offers the best approach toward achieving higher link linearity compared with directly modulated lasers since CW lasers with very low RIN noise are commercially available. Furthermore, the high output power of a laser can act "as an indirect RF power booster" for the RF input signal to provide a positive gain rather than a negative gain (or equivalent loss) [41]. This important feature adds advantage to the link using an external modulator compared with a directly modulated laser. *From this point forward of this book chapter, when we talk about the links or MPLs, we will specifically mean only externally modulated links*.

The quality of the overall links performance is largely measured by four important figures-of-merit [42], namely: (1) its dynamic range in terms of the spurious-free-dynamic-range (SFDR), (2) link gain (G), (3) noise figure (NF), and (4) bandwidth. The link gain (G) describes the relationship of the RF input signal power to RF output signal power of the IM-DD link, whereas the noise figure (NF) defines the signal-to-noise ratio (SNR) degradation in the link. The SFDR depicts the RF signal power range that can be accommodated by the link, taking into account the effects of noise and nonlinear distortions. It represents the highest signal to noise ratio when the intermodulation signal power is equal to the noise floor. Thus, it combines noise and linearity performance of the link. More detailed technical discussions on these figures-of-merit are found in references [14–16, 43].

The nonlinearities in any part of the links (such as laser, modulator, fiber, photodetector, amplifier, etc.) translate directly to signal noise and distortion. Nonlinear performance at the fiber occurs when the optical powers of the signals are high enough; hence, this is usually mitigated by proper engineering of the optical signal powers to avoid fiber-based nonlinearity. Similarly, detector nonlinearity is mitigated by proper optical power engineering so that the optical power impinging on the photodetector is within the linear response of the photodetector. The nonlinearity of the modulator affects the distortion and dynamic range of fiber optic links. From among these factors, the distortion produced by the external optical modulators has the most negative impact on the overall performance of the link. More specifically, the inherent nonlinear transfer function of the external intensity modulator is the dominant limitation in the performance of MPLs.

1.5. Adaptive linearized intensity modulator

As mentioned earlier, the major source of distortion in IMDD links is the nonlinearity of the intensity modulator. The quest to develop high linearity external modulator with wide bandwidth at low cost has been an on-going challenge for decades.

Besides linearity, other key and important attributes of an external intensity modulator include, (1) low half-wave (V_π) voltage, (2) low insertion loss (*IL*), (3) high bandwidth (*BW*) capability, (4) low-cost, and (5) low complexity design. The low V_π voltage is related to the slope of the transfer function of the modulator. In general, the steeper the slope of the transfer function of the modulator, the smaller the V_π voltage. The immediate impact is an increase of the link gain (G). A modulator with low V_π voltage, as well as low insertion loss, is very attractive since it lowers the necessary input power level of the link and increases gain. Thus, low V_π and low *IL* lead to higher dynamic range, and low noise figure (*NF*), while large bandwidth capability makes it better for high-end applications. Minimal complexity and low cost are interlinked and can open the use of high bandwidth **MPLs** applicable to more commercial applications.

Lastly, any linearized modulator must also have a high tolerance to changes in the RF power level, bias drifts, optical wavelength drifts, etc. This requirement calls for modulator with adaptive capability to provide better maintenance and stable operation of the overall MPLs.

Thus, the focus of this book chapter is two-fold. First, it provides a comprehensive overview of the different linearization approaches that have been proposed and implemented to obtain a highly linear external intensity modulator. Second, it reviews a special type of intensity modulator called interferometric modulator with phase-modulating and cavity-modulating components (IMPACC) that is not only highly linear but also adaptive. These combined features, as far as we know, are not available with any previously reported intensity modulators.

1.6. Objectives and organization

This chapter of the book is organized as follows. First, we give a brief outline of the different linearization technologies used for intensity modulator in Section 2. After a broad overview, we introduce the different optical approaches in linearizing the modulators. Then, we focus on one particular subgrouping known as MZI-based linearized modulator. In Section 3, we present a special type of MZI-based linearized modulator called IMPACC. IMPACC provides both superior linearity and unique adaptive feature. Here, we discuss its basic principle, configuration, and modeling. The comparison and discussion of the original IMPACC and ring-assisted Mach-Zenhder interferometer (RAMZI) modulator are also presented. In Section 4, we provide and analyze IMPACC and RAMZI's respective performances before giving our conclusion in Section 5.

2. Survey of linear intensity modulators

In this section, we discuss the different linear intensity modulators. Before presenting these modulators, we first discuss an important figure-of-merit called spurious free dynamic range (SFDR) which quantifies the linearity of a given link. In Section 2.1, we discuss its derivation using a 2-tone test and graphically describe its significance. In Section 2.2, we provide an overview of the different general techniques to linearize intensity modulators before focusing on one general approach called optical linearization in Section 2.3. Optical linearization has many implementation flavors depending on the particular optical structure used for the modulator. In Section 2.4, we narrow down to a subgroup known as MZI-based modulator because of its popularity and mature technology. Within this subgroup, there are different configurations that have been proposed and implemented, and we spotlight one configuration called IMPACC.

2.1. Measure of linearity: SFDR

A 2-tone frequency test is typically used to evaluate SFDR of the link. **Figure 3(a)** shows a typical IM-DD based MPL consisting of a laser, external modulator RF signal amplifier, optical fiber, photodetector, and RF output amplifier. Note that when the focus of the link is to establish the performance of the external modulator, the common practice is to consider only the intrinsic MPLs. Here, the calculation of dynamic range does not contain the effects of the optical fiber, electrical amplifiers, and optical amplifier, if present.

In **Figure 3(a)**, RF input signal with two closely spaced RF frequencies, f_1 and f_2, of equal-power levels, are simultaneously injected into a nonlinear external optical modulator. The nonlinear interaction between these two signals will create new output frequencies, as shown in the bottom portion of **Figure 3(a)**. Thus, the detected RF output signal will contain two fundamental frequencies, (e.g., f_1 and f_2) together with the second-order IMD output frequencies, (e.g., $f_1 + f_2$ and $f_2 - f_1$), second-order harmonics, (e.g., $2f_1$ and $2f_2$), and third-order IMD outputs (e.g., $2f_1 - f_2$ and $2f_2 - f_1$). Other higher order harmonics and IMD effects (e.g., fourth, fifth, etc.) can also be present, but their effects are generally small and can be filtered out. The second-order SFDR is only important for systems whose bandwidth is more than one octave because the second-order intermodulation products will fall outside the passband of a suboctave system. However, the most important and often most difficult to filter out are the third-order effects which occur very close to the fundamental frequencies within the system bandwidth of interest as shown in **Figure 3(a)**.

Instead of giving the mathematical derivation of SFDR and other relevant parameters or merits, we present a graphical treatment in the discussion of SFDR [16]. For detailed mathematical derivation, we direct readers to relevant references [14–16]. **Figure 3(b)** depicts the output RF

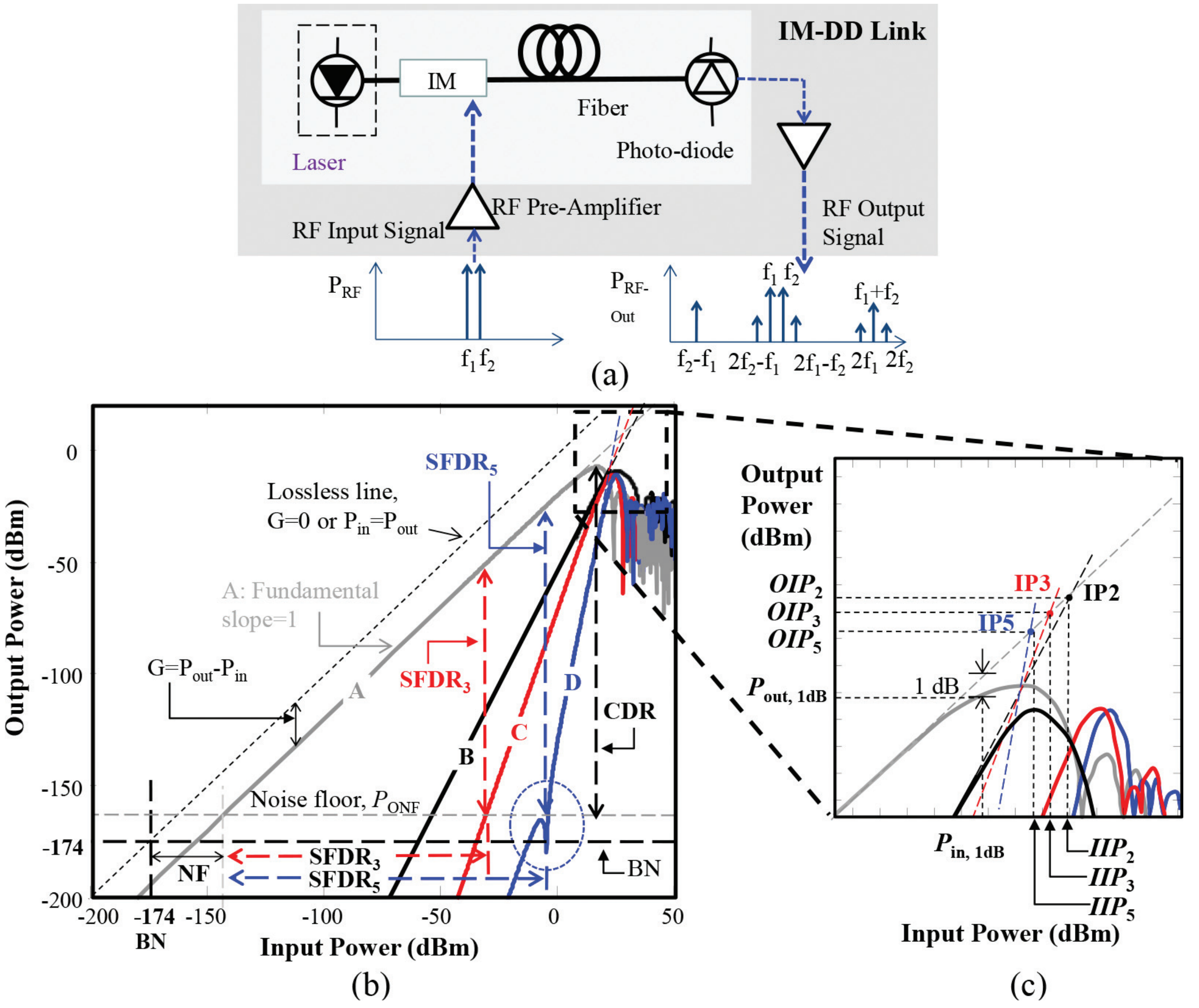

Figure 3. (a) Typical IMDD fiber optic link with input and output RF spectrum; (b) output RF power versus input RF power, showing the important MPL RF parameters/figures of merit, (A) fundamental curve with slope of 1, (B) second-order harmonics and intermodulation terms with slope of 2, (C) third-order intermodulation terms with slope of 3, (D) fifth-order intermodulation terms, with nonlinear slope and not the same slope in the entire frequency range, typical slope at the linear portion is 5 and corresponding SFDR calculations; (c) details of inset of (b) with the definition of the 1-dB compression point, and the *IPn*, with $n = 2, 3, 5$.

signal power versus the RF input power of the different frequency signals generated by the nonlinear interaction within the nonlinear external modulator. This single plot also demonstrates the relationships of the different parameters which we summarize below:

- **P_{ONF}, BN, P_{ON}, and P_{IN}:** P_{ONF} refers to the output noise floor, which is the minimum discernable signal, whereas ***BN*** is the background noise or thermal noise limit and equal to −174 dBm/Hz at a temperature of 25°C. P_{in} is the RF input signal power and P_{out} is the RF output signal power.

- **Link Gain, G:** The MPL gain, in dB, is defined as the difference of the power at the output of the MPL, P_{out}, to the available power of the input, P_{in} [16]:

$$G = P_{out} - P_{in} \tag{1}$$

We should note here that G is typically referred to as small signal gain, because only in the small-signal regime, the gain is independent of input signal power. That is, for any input power, the associated output power is G dB units higher than the input power. Hence, a straight line is obtained. However, as we continue to increase the modulation power (P_{in}), the straight gain line begins to saturate, until a maximum output power is reached and then starts curving downwards. Beyond this, any increase in the input power leads to lower output power. We should note that G is not necessarily positive. We use it here in its general form, where positive G means increase in the output power, whereas, negative G means reduction in the optical power or loss.

- **Different Signal Slope Lines:** The fundamental curve, third-order IMD curve, and fifth-order IMD curve have a slope of 1, slope of 3, and slope of 5 in the linear region, respectively. Note that oftentimes at the fifth-order IMD, the slope is not necessarily the same throughout the entire frequency band, but it can change from slope 3 to slope 5 [16, 44]. **Figure 3(b)** shows the associated slope lines marked as A (fundamental curve with slope of 1), B (second-order harmonics and intermodulation terms with slope of 2), C (third-order intermodulation terms with slope of 3), and D (fifth-order intermodulation terms, with nonlinear slope and not the same slope in the entire frequency range, typical slope at the linear portion is 5.

- **Noise figure (NF):**
 is defined as the 10 log(F), where F is the noise factor of the MPL and defined as the quotient of the signal-to-noise ratio (SNR) at the input to that at the output, taken for a thermal-noise-limited input at T_s or –174 dBm. Typically this is described by the following equation [16, 43]:

$$NF[dB] \equiv 10\ log(F) = 174 + N_{out}[dBm/Hz] - G[dB], \tag{2}$$

- **Spurious free dynamic range (SFDR):** Graphically, the SFDR is the difference measured from the corresponding point on the fundamental curve to the associated point in the intermodulation distortion (IMD) curve, where IMD intersects or equals the P_{ONF}. Physically, this means that this is the area for which any IMD terms are just below the noise floor and cannot be "seen" by the system. This approach determines the SFDR value, as discussed by Bridges et al. [45]. Mathematically, SFDR is defined as [45]:

$$SFDR = \frac{2}{3}\left(OIP3 - P_{ON} - 10\log_{10}(B)\right) \tag{3}$$

for a system limited by third-order IMD, where OIP3 is the output power at the third-order intercept point and B is the system bandwidth (with units Hz). It is simply two-thirds the difference between the largest distortion-less signal that can be input into the system and the smallest detectable signal in the system. The lower end of this range (the minimum discernable signal) is the sum of the output noise floor (P_{ONF}) and the system bandwidth, B. The measurement bandwidth is assumed to be 1 Hz. In this case, the units of SFDR are dB/Hz$^{2/3}$. However, in the case of more linear systems that are limited by fifth-order IMD, SFDR is mathematically defined as [45]:

$$SFDR = \frac{4}{5}\left(OIP5 - P_{ON} - 10\log_{10}(B)\right) \tag{4}$$

where OIP5 is the output power at the fifth-order intercept point. And, the units of SFDR for a system limited by fifth-order IMD are dB/Hz$^{4/5}$. These respective SFDRs for the third-order and fifth-order are labeled as SFDR$_3$ and SFDR$_5$, respectively in **Figure 3(b)**.

- **1-dB Compression point:** This is the point at which the small signal gain (e.g., straight extended line in **Figure 3(b)**) is 1-dB higher than the actual gain curve. This point signifies the end of the linear regime. A closer look of **1-dB Compression point** is depicted in **Figure 3(c)**.
- **Compression dynamic range (CDR)**: is the difference between the output power at the 1-dB compression point (expressed in dBm) to the smallest such input power (e.g., noise floor).
- ***IP*$_n$–*n*th-order intercept point**: If we extend the linear slope of the fundamental and the *n*th-IMD curve, then these lines intersect at a point. We called this point the *n*th-order intercept point (e.g., IP3 if the IMD is the third-order IMD curve, IP5 if the IMD is the fifth-order IMD curve). The point is defined by the input intercept power (IIP_n) and the output intercept power (OIP_n). These points are depicted in **Figure 3(c)**.

Note that in some new modulator designs, the fifth-order IMD curves are not always straight lines with a constant slope, but have a slight deviation from a straight line just above the noise floor. This is clearly seen in **Figure 3(b)**, in the circled region just below the output system noise level (P_{ONF}—output noise floor), where the slope of an IMD curve increases beyond 5. Since the nonlinearity in the IMD curve is not taken into account in Eqs. (3) and (4), the graphical approach is best suited to be used in calculating the SFDR for the new modulator. In this approach, the SFDR is simply defined as the difference between the fundamental and intermodulation output powers at the input power location where the IMD curve intersects the output noise floor (P_{ONF}).

2.2. Different linearization approaches

Figure 4 summarizes the three general approaches used to linearize a generic external intensity modulator based on the physical mechanism used, namely: (1) electrical, (2) optical, and (3) digital (post detection). The electrical and digital linearization approaches can further be subdivided into smaller categories (as in the case of optical linearization) but we will not review this in much detail here, however more detailed information can be found in [13, 21–22, 41, 46–55].

Briefly speaking, the electrical linearization approach employs different techniques [46–49] such as: (i) RF predistortion, (ii) RF Feed-forward, (iii) combined RF Feed-forward and predistortion, and (iv) others. These techniques generate circuits with either (a) inverse function

(ArcSin) of the modulator to predistort the RF signal before it is injected into the modulator, or (b) split a portion of the RF signal, amplify, reverse its sign, and add it to delayed original RF signal. The overall goal is to cancel or eliminate the original distorted components in the RF signal. These techniques are generally simple and inexpensive but they are limited by the frequency bandwidth of the electrical circuits [51, 53].

On the other hand, a digital linearization approach is based on the application of digital signal processing, DSP [50, 52, 54] techniques to post-detected output signal. The digital approach is very promising because of its flexibility and future growth of DSP. However, its practical usefulness will depend on the progress and development in analog-to-digital converter (ADC) and digital-to-analog converter (DAC) technologies. Unfortunately, ADC is limited by the sampling rate of <10 G/sample at this time [55]. Although there are ADC/DAC technology with >10 G/sample rates, they are usually for instrument purposes [55] and not for field deployment.

In contrast to electrical and digital linearization approaches, optical linearization is free from circuit frequency modulation limitation and does not utilize ADC/DAC technologies. For these reasons, we focus on the optical linearization approach in this chapter.

2.3. Optical linearization

As shown in **Figure 4**, the optical linearization approach can be subdivided further into 5 subgroupings, depending on the key optical structure of the modulator namely; (1) electroabsorption (EA) modulator [56–58], (2) directional coupler (DC) modulator [59–62], (3) all-optical-based approach [63–65], (4) ring resonator modulator [66–72], and (5) Mach-Zenhder interferometer (MZI)-based modulator [73–109]. These different modulators have been implemented and produced different varying degrees of linearity performance. From among these general configurations, the MZI-based modulator is the most well understood, most developed and popular optical structure in the technical community. Hence, we concentrate on the optical linearization approach with a focus on MZI-based linearized modulator.

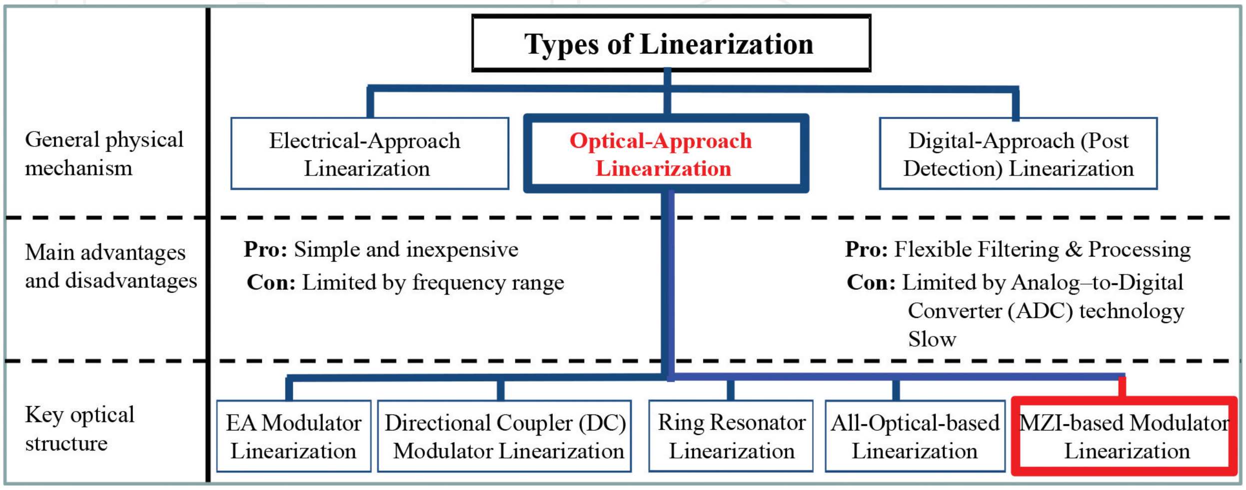

Figure 4. General classification of the different linearity approaches proposed/implemented in fiber-optics links.

2.4. MZI-based linearized modulator

Technically speaking, the MZI-based modulator is the most well-studied type of modulator. A typical nonlinearized MZI modulator has a SFDR value of around 90–112 dB-Hz$^{2/3}$. In the last decade, a wide range of linearization approaches has been proposed and implemented to improve the standard MZI modulator to have 120–130 dB-Hz$^{2/3}$ SFDR range using different configurations [74–76, 78–79, 81–84]. Recently, the goal is to push the SFDR further toward >130 dB-Hz$^{4/5}$. Nevertheless, most of them include complex designs and low modulation bandwidth.

Figure 5 shows these different types of MZI-based linearized electro-optic modulators, which can be divided into four groups depending on the actual implementations. The first group can be called dual-signal MZI-based modulator design [74–75, 83–84]. It comprises of one modulator but with two optical signals injected into the device, as depicted in **Figure 5(a)**. The two input signal amplitudes and phases must be properly matched with predetermined values of the RF amplitude phase signal. These two injected optical signals could be implemented using (i) two polarizations [74–75], (ii) two wavelengths [84], or (iii) bidirectional signals [83]. The major advantage of this family of modulators is the relative simplicity and low cost. Its disadvantages are design inflexibility, nonoptimum performance, and tight tolerance requirements.

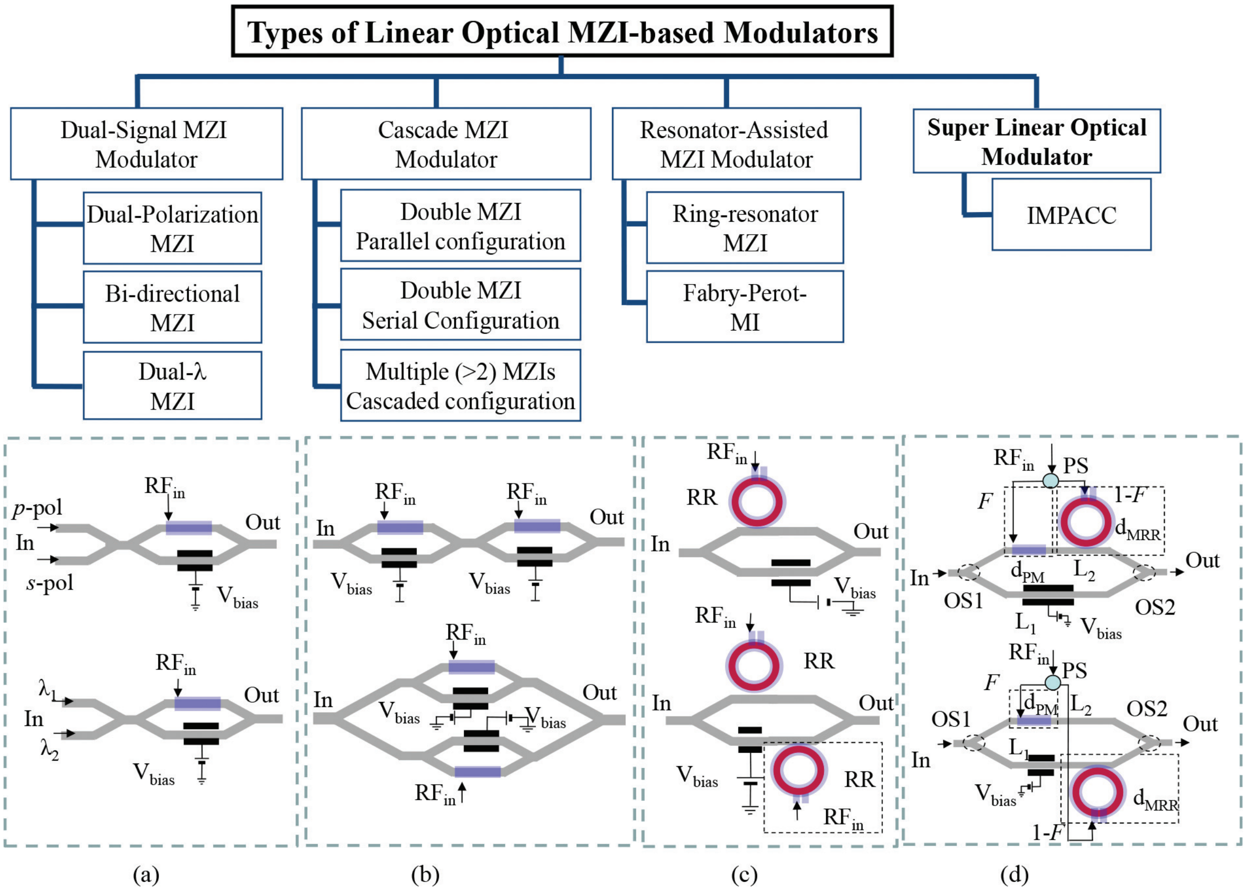

Figure 5. Different types of linear optical modulators based on MZI together with their respective implementation configurations for (a) dual-signal MZI modulator, (b) cascaded modulator, (c) RAMZI, and (d) IMPACC.

The second group can be referred to as cascaded modulator design which consists of two or more standard MZI modulators connected in series [76, 78–79, 80–82] or in parallel [100, 109] arrangements as illustrated in **Figure 5(b)**. It is a generalization of the principle used in the first group. Its major drawbacks are the tight manufacturing tolerance requirements, higher optical loss, higher cost, due to use of multiple modulators, and complicated compensation arrangement.

The third group is generally designated as RAMZI modulators [87–88, 97–99], which has received increased interest in recent years. Some implementations are shown in **Figure 5(c)**. The RAMZI uses ring resonator(s) (RRs) instead of the standard phase modulator (PM) which is coupled in the arm(s) of the MZI. This design gives higher SFDR performance but often at higher manufacturing complexity, limited RF bandwidth range, and stricter transmission coefficient control requirement.

The fourth and last group of optically linearized MZI-based modulators was introduced by our group [89, 93–94, 96, 101–105, 107–108]. This modulator design is a family of modulators which we referred to as **IMPACC**. There are numerous configurations and variations within the family of IMPACC designs [93]. Two of these implementations are shown in **Figure 5(d)**. One of these specific structures of IMPACC is discussed in more details in Section 3 and its performance in Section 4.

3. Design and modeling of IMPACC

This section discusses the basic principle, configuration, and modeling of IMPACC. In Section 3.1, we present an overview of IMPACC configuration. For both educational as well as clarity purposes, we identify the different elements of IMPACC and discuss them separately in Section 3.2. Lastly, we bring all these elements together to come out with IMPACC modulator. While this section gives the basic principle of IMPACC, Section 4 presents its performance.

3.1. Configuration of IMPACC

The configuration of our modulator, known as IMPACC, is shown in **Figure 6**. IMPACC comprises of a MZI configuration, in which one of its arms (e.g., lower) has an active microring resonator (MRR) modulator, whereas the other arm (upper) has an active phase modulator (PM). It uses the standard PM as the phase modulating component and the MRR as the cavity modulating component within a MZI structure [89, 93–94, 96, 101–108]. The exact positions of the PM and MRR relative to one another offer some variations of the implementation, as shown in **Figure 5(d)**.

Interestingly, the IMPACC configuration can be seen as a generalization of both MZI modulator and RAMZI. First, the normal combination of MZI structure and active PM in one of the arm of MZI leads to a typical *single-electrode MZ modulator*. Second, the typical combination of a MZI structure and an active MRR modulator in one of its arms results in a *single-electrode RAMZI modulator* [88, 91–92, 98]. When MRR and PM are present in MZI's arms, then this configuration becomes IMPACC.

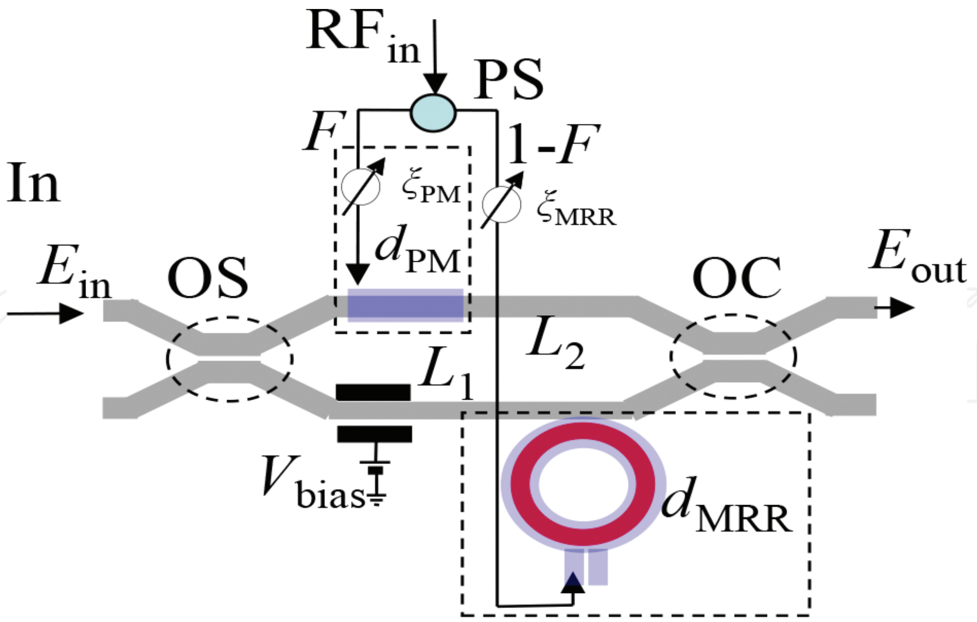

Figure 6. Basic configuration of IMPACC.

Another important aspect of IMPACC is that the RF power signal is split between the MRR and PM by the RF power splitter (PS) with a power split ratio of F:(1$-F$). This is a critical aspect in the operation of the IMPACC where PM and MRR are driven by the same frequency RF signal, but with different RF power, controlled by the power split ratio (F) using a variable or fixed RF power splitter (PS). Furthermore, the portions of the RF signals directed to MRR and PM electrodes are also delayed by an amount ξ_{MRR} and ξ_{PM}, respectively. These external control parameters from PS are not only instrumental in providing superior linear performance but also have key roles in delivering the unique adaptive mode of IMPACC. This adaptive feature is not available with any known modulators, as far as we know.

The input and output optical splitters (OS and OC) in the MZI configurations are generally assumed to have a (50:50) split so that the optical signal is divided equally into two portions. However, in this chapter of the book, we generalize this condition by taking OS and OC to have arbitrary optical power split ratios namely, P_{OS}:1$-P_{OS}$ and P_{OC}:1$-P_{OC}$. This condition allows us to investigate the effect of unbalanced power split ratio of OS and OC on the performance of IMPACC.

3.2. Elements of IMPACC

The details of the design of IMPACC have been previously described [77, 89, 93–94, 101–108]. Structurally speaking, IMPACC comprises of four important building blocks namely; (1) Mach Zehnder interferometer (MZI), (2) phase modulator (PM), (3) microring resonator (MRR) modulator, and (4) RF power splitter. In order to appreciate its rich properties, we will first briefly discuss the fundamentals of each of the four important constituents namely; (i) PM, (ii) MZM, (iii) RR, and (iv) RAMZI, before they are combined and operated under certain conditions to create IMPACC.

3.2.1. Phase modulator (PM)

The basic principle of phase modulators is based on the Pockels or linear electro-optic effect [73]. Depending on the material used, the specific axes orientations and the relative alignment of the incoming polarization to the index ellipsoid of the material used, the net effect is the refractive index modulation based on the external applied field. There are two typical configurations, the longitudinal electro-optic modulation and the transverse electro-optic modulation. In the first case, the electric field of the modulating field is parallel to the direction of the optical beam propagation (except near the edges of the electrodes). In the second case, the electric field of the modulating field is perpendicular to the direction of the optical beam propagation. This second case offers refractive index changes induced by the external electric field E that are proportional to the field E. Hence, the electrically induced phase change (or retardation) for the optical beam through the material is proportional to the product EL, where L is the length of the optical beam and electric field interaction and $E=V/d$ is the applied field, with V the applied voltage at the electrodes, which have a separation of d. The net effect is that the ratio L/d can be engineered large enough to provide devices which require low driving voltages.

Referring to **Figure 7**, an incident beam propagating along the y-direction, with polarization along the z-axis (typical case for $LiNbO_3$ based electro-optic devices), will experience an electrically induced phase change, φ_{pm} of [73]:

$$\phi_{PM} = \frac{2\pi}{\lambda} n_e L - \frac{\pi}{\lambda} n_e^3 r_{33} \frac{L}{d} V = \phi_0 - \Delta\phi, \tag{5}$$

where r_{33} is the electro-optic coefficients implicated in this crystal case and orientation [73], λ is the wavelength of the optical beam, n_e is the extraordinary index of refraction seen by the optical beam along this polarization orientation, L is the length of the crystal (or the interaction length of the optical and electric fields), and d is the separation of the electrodes. Note that the total phase change consists of two terms. The first one (e.g., ϕ_0) is the natural propagation phase change, whereas, the second term ($\Delta\phi$) is the electrically induced phase change. Because of the natural birefringence term, a phase compensator is required to adjust the phase until the total phase retardation in the absence of the electric field is an odd multiple of $\pi/2$. The half wave voltage for this case is [73]:

$$V_\pi = \frac{d}{L} \frac{\lambda}{n_e^3 r_{33}} \tag{6}$$

If the applied voltage V is sinusoidal $V = V_m \sin(\omega_m t)$, where ω_m is the modulation frequency and V_m is the applied magnitude of the voltage, then the transmitted beam will be phase modulated which can be expressed as [73]:

$$E_{(y,t)} = A \exp\left[j(\omega t - ky - \phi_0 + \delta \sin \omega_m t) \right] \tag{7}$$

where A is the constant amplitude, and the modulation index δ is given as [73]

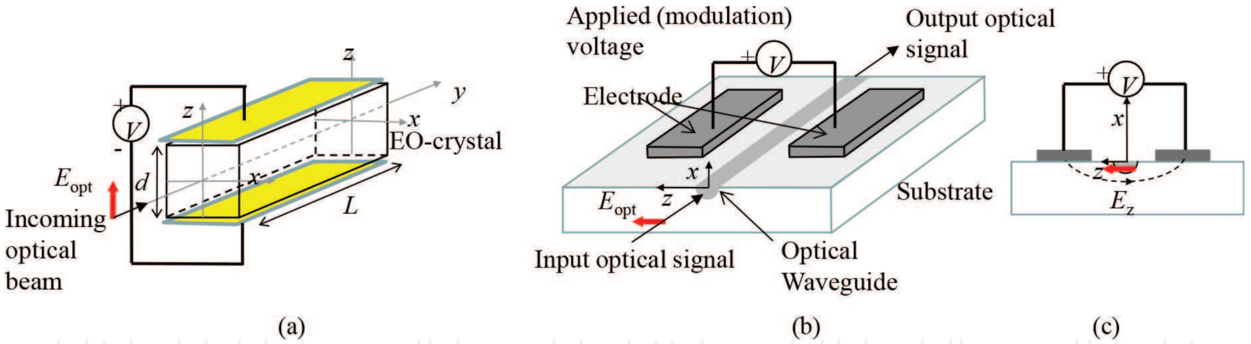

Figure 7. (a) Bulk electro-optic phase modulator, (b) photonic integrated waveguide electro-optic phase modulator in perspective view, (c) waveguide electro-optic phase modulator in cross-section view.

$$\delta = \pi \frac{L}{d} \frac{n_e^3 r_{33}}{\lambda} V_m = \pi \frac{V_m}{V_\pi} \tag{8}$$

We should note here that the phase modulator in a photonic integrated waveguide circuit is slightly different as it has to be modified to accommodate a substrate structure and the electrodes. A typical, but not the only, configuration is shown in **Figure 7(b)** and **(c)**. The optical waveguide is placed at the center of the gap between the two electrodes. In the optical waveguide, the direction of the field of the applied electric field is parallel to the substrate surface along the *z*-axis. The induced refractive index change Δn_z changes the phase in the way similar to Eq. 5.

3.2.2. Mach-Zehnder modulator (MZM)

A typical external modulator is usually in the form of an integrated optical modulator, which includes a waveguide MZI structure that is fabricated on a slab of lithium niobate ($LiNbO_3$). To ensure that light is channeled through the waveguide, the area is typically doped with impurities in order to increase the index of refraction.

Figure 8 shows a typical MZI modulator configuration where the incident light is split by a Y-branch optical splitrer (OS) into the two arms of the interferometer structure. The light traversing the first arm is modulated by a RF signal. As described in the previous section, the applied electric signal induces a change in the index of refraction of the first waveguide and hence the optical signal experiences a phase shift as it propagates through the waveguide. The magnitude of the phase delay is proportional to the applied voltage and is given by [14]:

$$\Delta\theta_{\mathrm{PM}} = \pi \frac{V}{V_\pi}, \tag{9}$$

where V is the voltage applied to the modulator and V_π is the half-wave voltage that when applied, causes a phase shift of π. The second portion of the splitted optical signal propagates into the second arm without RF modulation. Then, the two optical signals are recombined at the output by a Y-branch optical combiner (OC). This recombination can be either constructive

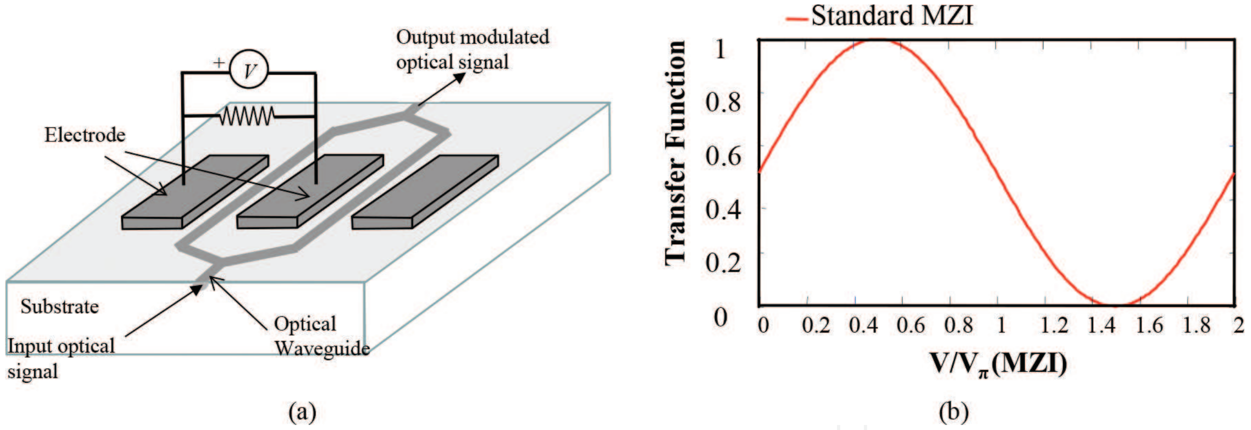

Figure 8. (a) Integrated electro-optic modulation using waveguide Mach-Zehnder Interferometer (MZI) structure, and (b) typical transfer function of a MZI.

or destructive depending on the relative phase difference of the two components of the interfering optical signals. Since the phase of one arm can be controlled by the applied electric signal, the output signal can be modulated. The transfer function of the MZI modulator is given by [73]:

$$T_{\mathrm{MZI}}(V) = \frac{1}{2}\left[1 + \cos\left(\pi\frac{V}{V_\pi} + \theta\right)\right], \tag{10}$$

where θ is the bias phase.

3.2.3. Single microring resonator (MRR)

The basic formulation for the physics of microring resonators (MRR) has been extensively discussed [85–86, 90]. We follow this analysis, in which an MRR has a total circumference length equal to d_{MRR} is coupled to a bus waveguide as shown in **Figure 9(a)**. The MRR round trip phase is given as $\theta_{MRR} = \omega{\cdot}n_0{\cdot}d_{\mathrm{MRR}}/c$, where n_0 is the index of refraction of the material, α is the loss factor of the MRR waveguide, and c is the velocity of the light.

In **Figure 9(a)**, the electric fields E_1, E'_1, E_2, and E'_2 are related by the matrix equation which describes their interactions as [91]:

$$\begin{pmatrix} E_2 \\ E'_2 \end{pmatrix} = \begin{pmatrix} \tau & -i\kappa \\ -i\kappa & \tau \end{pmatrix} \begin{pmatrix} E_1 \\ E'_1 \end{pmatrix} \tag{11}$$

where τ is the transmission coupling coefficient of the coupler between the bus waveguide and the MRR while κ is the associated cross coupling coefficient of the coupler. We assume that only a single mode of the MRR is excited, and the coupler is lossless, so that $\tau^2 + \kappa^2 = 1$.

The output electric field E_2, after *one* round trip, can be expressed as [91]:

$$E_2 = \tau E_1 - i\kappa E'_1 = \tau E_1 - (i\kappa)\alpha e^{-i\theta_{\mathrm{MRR}}} E'_2 = \tau E_1 - (i\kappa)^2 \alpha e^{-i\theta_{\mathrm{MRR}}} E_1 = (\tau - \kappa^2 \alpha e^{-i\theta_{\mathrm{MRR}}}) E_1 \tag{12}$$

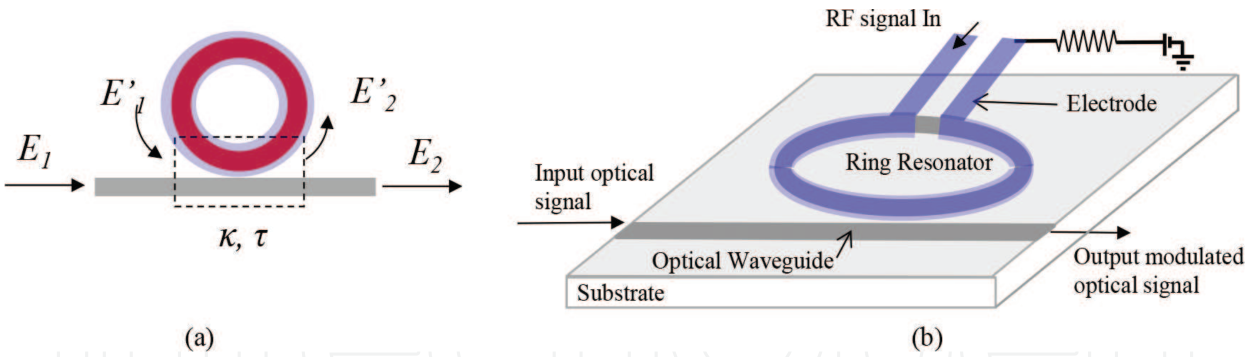

Figure 9. Microring Resonator (MRR) with one bus waveguide, (a) top view showing the field amplitudes at the input and output of the coupling region, (b) perspective view of the MRR with RF electrode.

Here, α is the RR waveguide loss factor ($\alpha = 1$ indicates that the RR is lossless).

After *two* roundtrips, we have [91]:

$$E_2 = (\tau - \kappa^2 \alpha e^{-i\theta_{\text{MRR}}} E_1 - \kappa^2 \tau \alpha^2 e^{-i2\theta_{\text{MRR}}}) E_1 \tag{13}$$

Repeating this circulation around the MRR n times, output electric field E_2 leads to [91]:

$$E_2 = \left[\tau - \kappa^2 \sum_{n=1}^{\infty} \tau^{n-1} \left(\alpha e^{-i\theta_{\text{MRR}}} \right)^n \right] E_1 \tag{14}$$

And finally, after infinite roundtrips, we have got the output electric field E_2 as [91]:

$$E_2 = \frac{\tau - \alpha e^{-i\theta_{\text{MRR}}}}{1 - \tau\alpha e^{-i\theta_{\text{MRR}}}} E_1 \tag{15}$$

Thus, its corresponding normalized transmission transfer function $T_{MRR}(\theta)$ under steady-state condition is given by [91]:

$$T_{\text{MRR}}(\theta) = \left| \frac{E_2}{E_1} \right|^2 = 1 - \frac{(1-\alpha^2)(1-\tau^2)}{(1-\alpha\tau)^2 + 4\alpha\tau \sin^2(\theta_{\text{MRR}}/2)} \tag{16}$$

Accordingly, the corresponding phase response, Θ_{MRR} and group-delay (GD) [95] response of MRR can be derived as [110, 111]:

$$\Theta_{\text{MRR}} = \pi + \theta_{\text{MRR}} + \arctan\left[\frac{\tau \sin(\theta_{\text{MRR}})}{\alpha - \tau \cos(\theta_{\text{MRR}})} \right] + \arctan\left[\frac{\alpha\tau \sin(\theta_{\text{MRR}})}{1 - \alpha\tau \cos(\theta_{\text{MRR}})} \right] \tag{17}$$

$$GD = -\frac{d}{d\omega} [\Theta_{\text{MRR}}] \tag{18}$$

Eqs. (14) and (16) will be handy in the analysis of the new modulator that we discuss in Section 4.

(A).Passive (steady-state) operation

The relationship between the magnitude of the bus waveguide-to-MRR transmission coupling coefficient (τ) and the RR waveguide loss factor (α) defines the three different coupling conditions of MRR [73, 85, 91, 110–112]. **Figure 10(a)** shows the typical MRR while **Figure 10(b)** depicts its three different operating coupling conditions known as (1) critical-coupled (CC) when $\alpha = \tau$, (2) over-coupled (OC) when $\alpha > \tau$, and (3) under-coupled (**UC**) when $\alpha < \tau$. Their respective intensity and phase responses are shown in **Figures 10(b)** and **(c)**, respectively. One notable observation in **Figure 10(b)** is that the intensity output becomes zero at resonance frequency (normalized frequency $\Omega = 0$) under CC condition. In comparison, the respective dip intensity outputs of OC MRR and UC MRR are always higher than zero. The second significant observation is found in **Figure 10(c)** where the phase response of UC MRR is "opposite in direction" compared with phase responses of both OC MRR and CC MRR. This is significant and is used in many group-delay/chromatic dispersion mitigation approaches. Recall that if waveguide lossfactor $\alpha = 1$, then MRR is ideally lossless and becomes an all-pass filter or phase only filter.

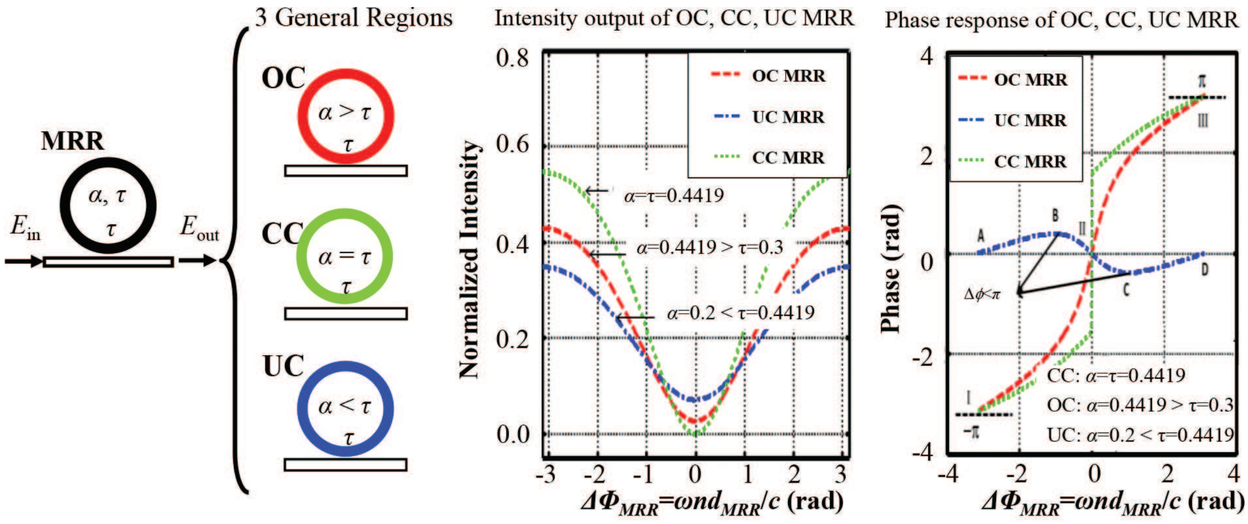

(a) (b) (c)

Figure 10. (a)The three different operating coupling conditions of MRR under critical-coupling (CC) at $\alpha = \tau$, over-coupling (OC) at $\alpha > \tau$, and under-coupling (UC) at $\alpha < \tau$ conditions, (b) normalized intensity response for the three operation conditions, and (c) their respective phase responses for the three operation conditions.

(B). Dynamic operation

If a voltage V, is applied to an electro-optic (EO) MRR, a corresponding round-trip phase shift θ_{MRR} induced in the ring resonator is then given as [73]:

$$\theta_{MRR} = \theta_0 + \Delta\beta \cdot d_{MRR}, \tag{19}$$

where $\theta_0 = \omega n\, d_{MRR}/c$ is the static MRR phase response, and

$$\Delta\beta = \frac{\pi n_0^3 r \Gamma V}{\lambda g}. \tag{20}$$

The parameter $\Delta\beta$ is responsible for the dynamic phase change due to applied voltage. Here, r is the electro-optic coefficient of the waveguide, λ is the incident light wavelength, g is the electrode gap and Γ is the overlap integral.

For a sinusoidal voltage, $V=V_0 \sin \omega_m t$ applied to the MRR, then using the same approach that was used to derive Eq. (14), the output amplitude, $E_{\text{out}}(t)$ is given by [77] :

$$E_{out}(t) = \left[\tau - \kappa^2 \sum_{n=1}^{\infty} \tau^{n-1} \alpha^n \exp\left[-i\left(n\theta_{\text{MRR}} + \delta_n \sin(\omega_m t - n\phi)\right)\right]\right] E_{in}(t) \tag{21}$$

where $\phi = \omega_m/FSR$ with ω_m being the modulation frequency and FSR is the free spectral range of MRR, n is the number of round trip around the ring, and δ_n is the modulation index. The modulation index depends on the electrode structure. For a lumped electrode, the modulation index is [91–92]:

$$\delta_n \sin(\omega_m t - n\phi) = \int_0^{nL} \Delta\beta \sin\left[\omega_m\left(t + \frac{n_0}{c}z\right) - n\phi\right] dz = \Delta\beta d_{\text{MRR}} \frac{\sin(n\phi/2)}{\phi/2} \sin(\omega_m t - n\phi) \tag{22}$$

For a traveling wave electrode, the modulation index is given by [91–92]:

$$\begin{aligned} \delta_n \sin(\omega_m t - n\phi) &= \sum_{k=0}^{n-1} \int_0^{nL} \Delta\beta \sin\left[\omega_m\left((t + kt_r) - \frac{\Delta n}{c}z\right) - n\phi\right] dz \\ &= \Delta\beta d_{\text{MRR}} \frac{\sin(\psi/2)}{\psi/2} \frac{\sin(n\phi/2)}{\sin(\phi/2)} \sin\left(\omega_m t - \frac{\psi}{2} - \frac{n+1}{2}\phi\right) \end{aligned} \tag{23}$$

Where $t_r = n_0 L/c$ is the optical round-trip time and $\psi = \omega_m \cdot \Delta n \cdot d_{MRR}/c$ is the velocity matching factor. Here, $\Delta n = n_m - n_0$, where n_m is the microwave effective index and n_0 is the optical index.

3.2.4. RAMZI

Figure 11(a) illustrates a RAMZI configuration where MRR is coupled to a MZI in one of its arms. We assumed that the OS and OC of the MZI have balanced (50:50) power split ratios. Then, the transfer function of RAMZI is given as [66–67, 91–92, 98]:

$$T_{RAMZI}^{SS}(\theta) = \frac{1}{2}\left|\left[\frac{1}{\sqrt{2}}|a(\theta_{\text{MRR}})| e^{-iArg[a(\theta_{\text{MRR}})]} + \frac{1}{\sqrt{2}} e^{-i\phi_{\text{MZI}}}\right]\right|^2, \tag{24}$$

where $\alpha(\theta_{MRR})$ is the complex amplitude transfer function of the MRR under steady-state (SS) condition, which is given by Eq. (14) or (15), the phase response of MRR, $\Theta_{\text{MRR}} = \text{Arg}[\alpha(\theta_{MRR})]$ is given by Eq. (17), and ϕ_{MZI} is the DC phase bias between the two arms of the MZI. In Eq. (24), we assumed that the nominal MZI-arm lengths L_1 and L_2 are equal, except for the length due to DC phase bias. If the MRR is lossless ($\alpha = 1$), $\tau = 2 - \sqrt{3}$ and $\phi_{MZI} = \pi/2$, then

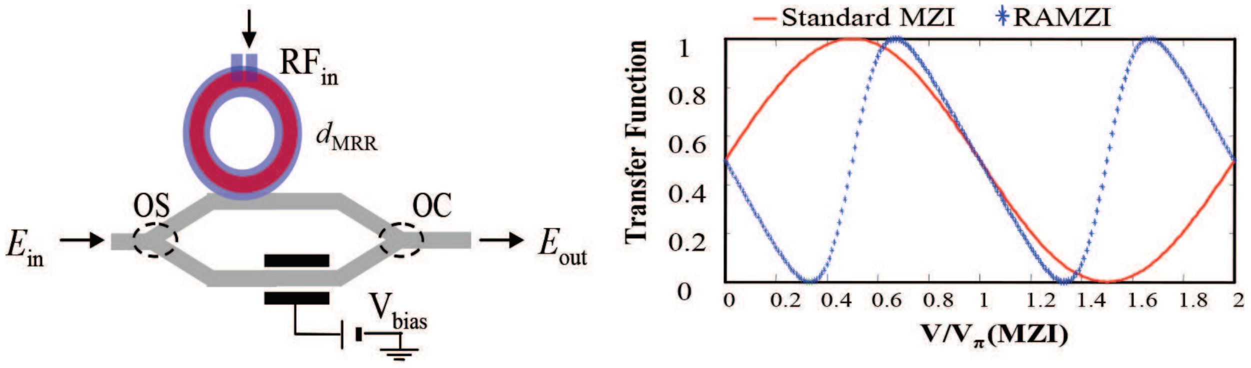

(a) (b)

Figure 11. (a)Schematic of RAMZI, and (b) typical transfer function of a RAMZI under steady state condition in comparison with standard MZI.

RAMZI becomes linearized around $\theta = \pi$, which is off-resonance for the MRR [66–67, 91–92, 98]. **Figure 11(b)** shows the typical linearized transfer function of RAMZI in comparison to standard MZI output intensity profile.

On the other hand, under dynamic state (DS) where a modulating sinusoidal RF voltage V is applied to MRR electrode, the corresponding transfer function of RAMZI is given as [91]:

$$T^{DS}_{RAMZI}(\theta) = \frac{1}{2}\left|\frac{1}{\sqrt{2}}|a(\theta_{\mathrm{MRR}})|\exp\left[-i\left(\arg[a(\theta_{\mathrm{MRR}})]+kn_0L_2\right)\right]+\frac{1}{\sqrt{2}}\exp\left[-i(kn_0L_1+\theta_{\mathrm{bias}})\right]\right|^2, \tag{25}$$

where $\alpha(\theta_{MRR})$ is given by Eq. (21), θ_{bias} is the phase bias of MZI and [91]

$$\theta_{\mathrm{MRR}} = n(kn_0d_{\mathrm{MRR}}) + \Delta\beta d_{\mathrm{MRR}}\frac{\sin(n\phi/2)}{\sin(\phi/2)}\sin\left(\omega_m t - \frac{(n+1)\phi}{2}\right). \tag{26}$$

for a lumped electrode case. The dynamic performance of RAMZI will be shown in Section 4 together with IMPACC performance side-by-side for clear comparison.

3.3. IMPACC

As described briefly in Section 3.1, IMPACC is a generalization of standard MZI modulator and RAMZI. **Figure 12(a)** shows the IMPACC configuration (a) together with its linearized transfer function (b) under its steady-state condition. Here, we assume that both OS and OC have 50:50 optical power split ratios, although later we will relax this restriction and consider arbitrary optical power split ratios namely, P_{OS}:$(1-P_{\mathrm{OS}})$ and P_{OC}:$(1-P_{\mathrm{OC}})$.

Structurally speaking, IMPACC is very much like the RAMZI configuration except for two big differences. First, the passive path-difference, ΔL of the MZI in the RAMZI modulator is now replaced by an active phase modulator (PM) element. Second, the total RF signal driving the electrode in MRR for RAMZI is now split into two portions, by a ratio of F:$(1-F)$, and drives both the electrodes of MRR and PM elements of IMPACC. The two split RF signals are also

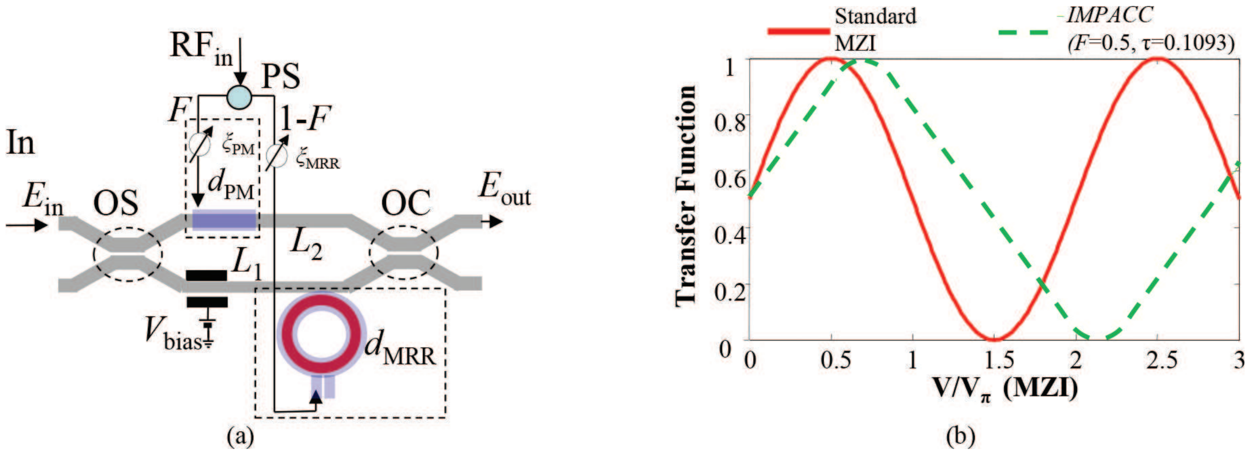

Figure 12. (a) IMPACC configuration, and (b) its transfer function in comparison with standard MZI.

delayed by an amount ξ_{MRR} and ξ_{PM}, respectively. The external control of the RF power split ratio F:(1−F) adds a degree of freedom in the design and serves to drive both the PM and MRR under specific power ratios. The corresponding linearized transfer function of IMPACC under its steady-state condition is shown in **Figure 12(b)**. Here, we assume that both OS and OC have 50:50 optical power split ratios although later in Section 3.3.1, we will relax this restriction by taking optical power split ratios namely, P_{OC}:(1−P_{OC}) to have 50:50 split while OS has arbitrary split of P_{OS}:(1−P_{OS}).

3.3.1. Transfer function

The dynamic transfer function of IMPACC, $T^{DS}{}_{IMPACC}(\theta)$ is given as [104]:

$$T^{DS}_{IMPACC}(\theta) = \frac{1}{2}\left|\sqrt{p_{MRR}}|a(\theta_{MRR})|\exp\left[-i(\arg[a(\theta_{MRR})] + kn_0L_2)\right] + \sqrt{p_{pm}}\exp\left[-i\left(\varphi_B + kn_0L_1 + \theta_{pm}\right)\right]\right|^2 \tag{27}$$

where

$$a(\theta_{MRR}) = \tau - \kappa^2\sum\nolimits_{l=1}^{\infty}\tau^{n-1}\alpha^n\exp\left[-i\theta_{MRR}\right] \tag{28}$$

$$\theta_{MRR} = n(kn_0d_{mrr}) + \sqrt{1-F}\Delta\beta d_{MRR} + \sqrt{1-F}\Delta\beta d_{MRR}\frac{\sin(n\phi/2)}{\sin(\phi/2)}\sin\left(\omega_m t + \xi_{mrr} - \frac{(n+1)\phi}{2}\right) \tag{29}$$

and

$$\theta_{pm} = kn_0d_{pm} + \sqrt{F}\Delta\beta d_{pm} + \sqrt{F}\Delta\beta d_{pm}\sin(\omega_m t + \xi_{pm} - \phi) \tag{30}$$

The parameters p_{MRR} and p_{PM} are the input optical power split ratio coefficients of the input optical splitter (OS) for the MRR and the PM arms, respectively. Note that $p_{MRR} = 1 - P_{OS}$, $p_{PM} = P_{OS}$, where P_{OS} was defined in Section 3.3. Also, here we assumed that OC has 50:50

power coupling ratio. The parameters θ_{pm} and $\arg[a(\theta_{MRR})]$ are the phase responses of the PM and MRR respectively, while the parameters d_{PM} and d_{MRR} are the lengths of the PM and MRR, respectively with n being the number of times the beam propagates inside the MRR, ω_{m} is the modulation frequency, $\phi = \omega_{\mathrm{m}}/FSR$, φ_B is MZI optical bias phase, ξ_{MRR} and ξ_{PM}, are the RF signal phase biases injected to the MRR and PM electrodes, respectively, and $\Delta\beta$ is given by Eq. (20). We assume negligible microwave loss and no velocity mismatch.

Unlike RAMZI, IMPACC has an external control of either the RF power split ratio or the RF bias. As we will show in the next section, while both of these modulator designs can result in high SFDR performance, IMPACC has an additional and unique property—an adaptive, inherent compensation capability that can be used to maintain its high SFDR under three nonideal parameter conditions namely: (1) increasing MRR waveguide loss factor, (2) unfavorable MRR coupling operating conditions, and (3) unbalanced input power split ratios of either the optical splitter, OS or optical combiner, OC. This adaptive property provides an additional level of design flexibility and can greatly simplify the overall operation of high-performing modulator.

4. Performance of IMPACC

This section provides details of the linearity performance of IMPACC in terms of SFDR, and compares it with RAMZI and standard MZI modulators. Unlike RAMZI and MZI modulators, IMPACC modulator has two different operational modes, namely: (i) the typical basic mode, and (ii) the unique adaptive mode. As far as we know, IMPACC is the only intensity modulator that has an adaptive mode. In Section 4.1, we focus on its basic operating mode, whereas in Section 4.2 we discuss the adaptive mode.

4.1. Basic operating mode of IMPACC

In the basic mode, IMPACC operates under fixed, predetermined parameter conditions aimed to optimize its performance. This mode of operation is typical in all intensity modulators. Here, we investigate the effects of the different parameter variations (from these optimum conditions) on IMPACC's SFDR performance, as well as its bandwidth capability, to assess its performance limits. These parameters include (i) MRR loss factor α, (ii) τ and α that define the CC, UC, and OC conditions, and (iii) unbalanced power split ratio (e.g., P_{os}:$(1-P_{\mathrm{os}})$) of optical splitters (OS). We also compare IMPACC performance with RAMZI and standard MZI modulators.

4.1.1. Effect of ring resonator's loss on SFDR

Any MRR waveguide has an intrinsic loss, (expressed as loss factor, α in Section 3). Here, we assess its effect on both IMPACC and RAMZI's SFDR performance [104]. **Figure 13(a)** shows the respective SFDRs of both IMPACC and RAMZI under two conditions; (a) an ideal lossless MRR waveguide (e.g., $\alpha = 1.0$), and (b) lossy case (e.g., $\alpha = 0.8$). Note that parameter τ is chosen for both IMPACC and RAMZI to get their respective highest SFDR values. We choose to use $\tau = 0.6355$ for

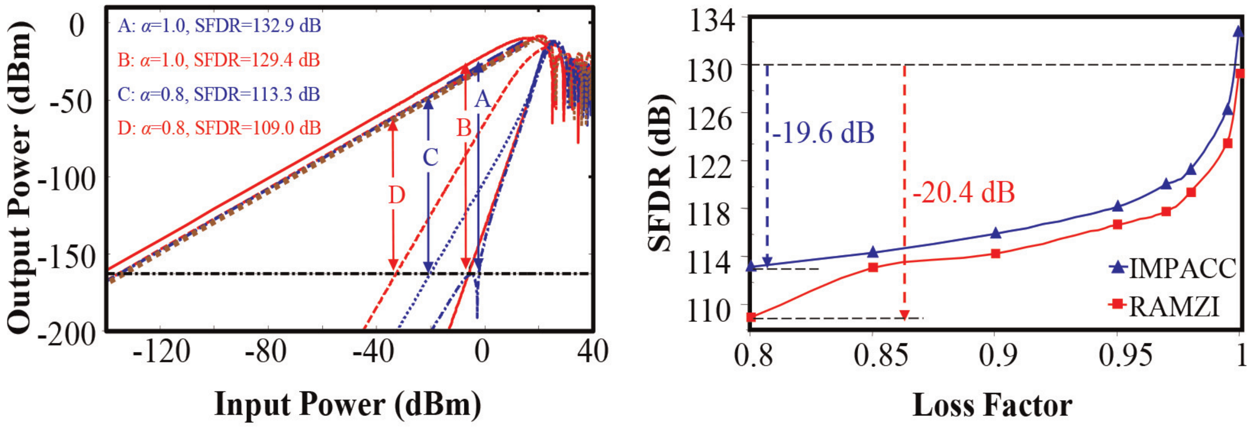

(a) (b)

Figure 13. (a) Effect of MRR waveguide loss, α on the SFDRs of IMPACC and RAMZI for $\omega_m = 1$Hz (F, ξ_{PM} are fixed), (A) IMPACC with $\alpha = 1$, (B) RAMZI with $\alpha = 1$, (C)IMPACC with $\alpha = 0.8$, (D) RAMZI with $\alpha = 0.8$; (b) effect of different values of MRR loss factor on the SFDR values for IMPACC and RAMZI.

IMPACC and the ideal value of $\tau = 0.2679$ for RAMZI. Furthermore, the modulation frequency, ω_m is set to 1 Hz, while the power split ratios of OS and OC are assumed both balanced (50:50). Here, we see that IMPACC has an SFDR value of 132.9 dB under lossless condition (labeled as A) that reduces drastically to 113.3 dB (labeled as C) when loss is introduced. A similar pattern is observed for the RAMZI case, where its SFDR value deteriorates from 129.4 dB for lossless case (labeled as B) to 109.0 dB for lossy case (labeled as D).

Figure 13(b) summarizes the full effect of MRR loss factor α on the SFDR of both IMPACC and RAMZI when the value of α is allowed to vary from 1 to 0.8. We have the following three observations. First, the respective SFDR performances of IMPACC and RAMZI are affected drastically and negatively by the decreasing value of the MRR loss. It is clear from **Figure 13(b)** that the MRR loss value must be minimized within $a < 0.99$ to obtain the higher than 126 dB-Hz SFDR performance. Second, IMPACC always outperforms RAMZI. It exhibits a consistently higher SFDR value (e.g., more than 1 dB) compared than RAMZI for the range $a = 1$ to $a = 0.85$. Third, at the range of $a = 0.85 – 0.80$, the SFDR performance of RAMZI degrades more than three times compared with IMPACC. The comparative SDFR difference between IMPACC and RAMZI increases from 1.2 dB when $a = 0.85$ – 4.3 dB with $a = 0.8$. This implies that IMPACC has a higher parameter tolerance to MRR loss variation especially at higher loss condition.

4.1.2. Effect of OC, UC, and CC operating conditions on SFDR

The SFDR performance of any MRR-based devices, including IMPACC and RAMZI, depends highly on the relative ratio between the MRR coupling coefficient strength (τ) and intrinsic loss factor (a) As mentioned in Section 3, there are three MRR regions of operation namely; (i) over-coupling (OC) condition, when $a > \tau$, (ii) critical coupling (CC) when $a = \tau$, and (iii) under-coupling (UC) when $a < \tau$.

Here, we selected the three regions with the following parameters; (i) OC condition ($\tau = 0.6364$, $\alpha = 0.7364$), (ii) CC condition ($\tau = 0.6364$ and $\alpha = 0.6364$), and (iii) UC condition ($\tau = 0.6364$ and

$\alpha = 0.5364$). Note again that we choose $\tau = 0.6364$ for IMPACC and the ideal value of $\tau = 0.2679$ for RAMZI. Furthermore in order to simplify the analysis and gain better understanding of the different parameter effects, we assumed an ideal, balanced 50/50 power split ratio for both the input optical splitters (OS) and output optical combiner (OC). The effect on nonideal 50:50 split ratio of OS will be discussed in the next section. Moreover, we assumed that IMPACC and RAMZI are driven at one of its resonant modulation frequency of 23 GHz.

Briefly speaking, the SFDR performance of both IMPACC and RAMZI under OC condition is shown in **Figure 14(a)**. IMPACC has superior linearity with SFDR =130 dB which is far better than RAMZI (e.g., 110 dB). This superior SFDR value is maintained (e.g., 129.7 dB) under CC condition as shown in **Figure 14(b)**. Lastly, the SFDR performance of both IMPACC and RAMZI under UC condition is also shown in **Figure 14(c)**. Under UC condition, both IMPACC and RAMZI are no better than the typical nonlinearized MZI modulator having SFDR value in the range of 110–113 dB. However, we can state that IMPACC's SFDR value (e.g., 113 dB) is still 3 dB higher when compared with RAMZI (e.g., 110 dB). Thus, the takeaway from **Figure 14** is that the huge SFDR advantage of IMPACC to RAMZI exists only when MRR is operated either in OC or CC condition.

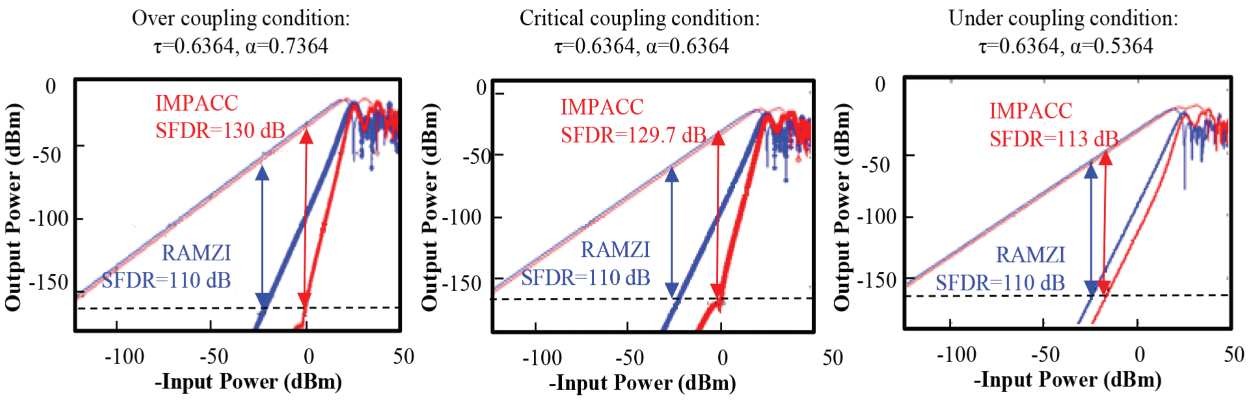
Over coupling condition: τ=0.6364, α=0.7364

Critical coupling condition: τ=0.6364, α=0.6364

Under coupling condition: τ=0.6364, α=0.5364

(a) (b) (c)

Figure 14. SFDR performance at (a) over-coupling, (b) critical-coupling and (c) under-coupling condition for 23 GHz modulation frequency (analysis assumes a resolution BW of 1 Hz).

4.1.3. Effect of unbalanced optical coupler on SFDR

This section studies the effect on nonideal, unbalanced split ratios of the optical splitter (OS) or optical combiner (OC) on the SFDR performance of IMPACC for three different MRR operating conditions (OC, UC, CC) [110]. To simplify the analysis, we limit our study to unbalanced OS by maintaining OC to have 50:50 power split ratio. Note that we use the same parameters as found in Section 4.1.2 with $\tau = 0.6364$ for IMPACC and the ideal value of $\tau = 0.2679$ for RAMZI.

4.1.3.1. Over-coupled (OC) IMPACC

Figure 15(a) shows the effect of the unbalanced power split ratio (e.g., 55:45) of OS on SFDR performance of IMPACC. The SFDR value drops by 6 dB from 130 dB-Hz under balanced condition to 124 dB-Hz under unbalanced case. **Figure 15(b)** depicts the SFDR performance for various split ratios. It is plotted as a function of the offset from the ideal optical splitter balanced condition (0 deviation corresponds to an ideal power split ratio of 50:50) to a very unbalanced condition (e.g., 0.20 corresponds to power split ratio of 70:30 and −0.20 corresponds to power split ratio of 30:70). One conclusion from **Figure 15(b)** is that in order to maintain a SFDR value of above 124 dB-Hz, we need to ensure that the OS power split ratio deviation should be no greater than ± 0.08 or no more than 58:42 or 42:58 power split ratio. Note that the results of **Figure 15(b)** were obtained without changing any external IMPACC parameters (e.g., RF power split ratio-F or the RF phase bias-ξ_{PM}) except the coupling ratio OS.

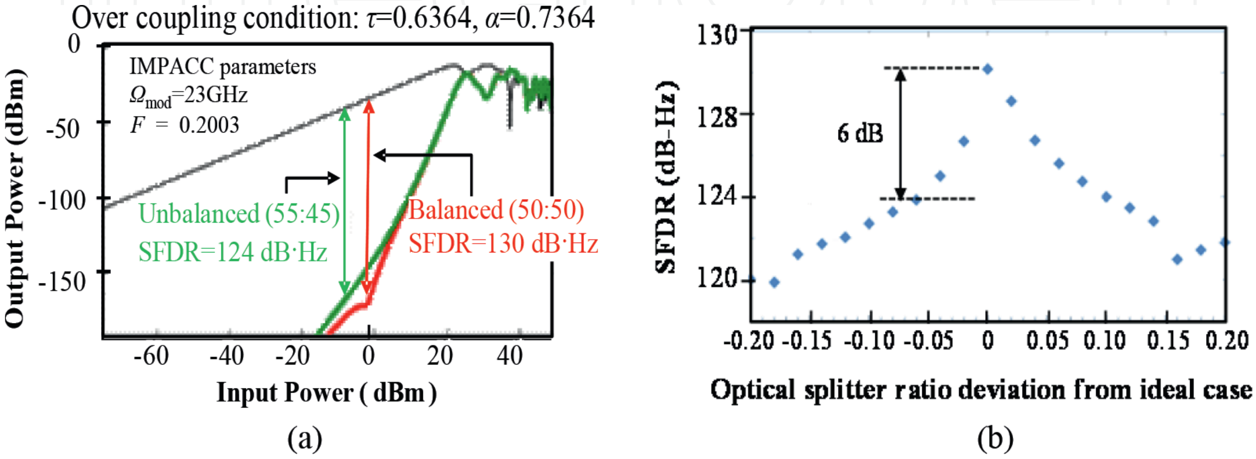

Figure 15. (a) SFDR degradation due to particular unbalanced optical power splitter (55:45) when MRR is operated under over-coupling condition, (b) SFDR performance for different unbalanced optical power split ratios.

4.1.3.2. Critical-coupled (CC) and under-coupled (UC) IMPACC

Figure 16 shows IMPACC's SFDR performance under (a) CC and (b) UC conditions for balanced (i.e., 50:50) and unbalanced (e.g., 55:45) cases. We see that the SFDR value of the OC condition degrades by 11 dB from balanced case of 129 dB-Hz to 118 dB-Hz for unbalanced case. Compared with the OC case (**Figure 15a**) where the SFDR drops only by 6 dB, the CC condition implies higher sensitivity to OS split ratio deviation. On the other hand, **Figure 16(b)** illustrates that OS split ratio deviation has no effect in the balanced or unbalanced cases for UC condition. However, IMPACC has only low SFDR value of 113dB-Hz.

4.1.4. SFDR versus modulation bandwidth response of IMPACC

We know that the modulation bandwidth of all ring resonator based modulators, such as RAMZI and IMPACC is typically limited by the MRR's free-spectral range (FSR) [91, 102, 104–105]. Here, we describe the SFDR-vs-modulation bandwidth capability of both IMPACC and RAMZI, and assess their respective performance limits. We evaluate the SFDR-vs-modulation bandwidth under lossless case (A), and under the three MRR operating conditions (B).

4.1.4.1. MRR lossless case (OC Condition)

Here, we assume that the loss factor a in the MRR waveguide, for both the IMPACC and the RAMZI, is lossless or equal to 1. Although, this is not a realistic case, it is done to focus on the

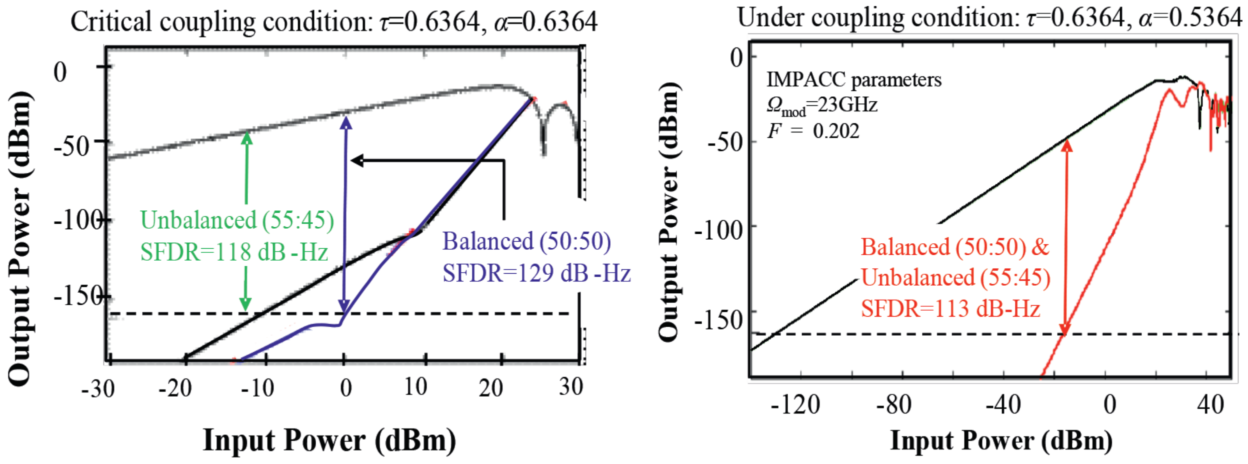

(a) (b)

Figure 16. SFDR of IMPACC at over-coupling condition (a), and under-coupling condition (b) for both unbalanced and balanced scenarios (modulation frequency 23 GHz, $\xi_{PM} = 1.3893\pi$, $F = 0.2008$).

bandwidth capability and understand its performance limits. Later in the next subsection, we consider the effect of MRR loss. Here, we use $\tau = 0.208$ for IMPACC, $\tau = 0.268$ (or $\tau = 00.2679$) for RAMZI [90–91, 95, 104], MRR RF phase bias $\xi_{MRR} = 0_,$ and a PM RF bias control sensitivity ξ_{PM} of 0.2° [105]. The two τ values have been selected such that they provide maximum SFDR value for each case.

First, **Figure 17(a)** shows the SFDR-vs-Modulation frequency of IMPACC (blue line), RAMZI (red line), and MZI modulator (green line) for modulation frequencies up to 75 GHz. IMPACC has an increasingly higher SFDR, (e.g., 3.7 dB to 13.7 dB) compared with RAMZI and standard MZI modulators for these increasing resonant frequencies. It is important to note that the resonance enhancement in IMPACC is accomplished without resorting to a smaller ring size. Smaller ring size not only makes the fabrication more challenging, but would also introduce larger resonator waveguide losses.

Next, we identify two frequency regions of operation: (i) the resonance region at around ~23 GHz (shown in **Figure 17(b)** and ~70GHz (shown in **Figure 17(c)**), and (ii) the non-resonance region at around 56 GHz (shown in **Figure 17(d)**) [105]. The resonance region is defined as the region where the SFDR is greater than that obtained from an ideal MZI, which has a relative flat response as a function of frequency. These resonant regions occur at multiples of the FSR of the modulator (e.g., 23.3 GHz, 69.9 GHz).

As shown in **Figure 17(a)**, IMPACC provides an increasingly higher SFDR, (e.g., 3.7 dB to 13.7 dB) compared with RAMZI and MZI at these resonant frequency regions. **Figures 17(b)** and **(c)** depict the respective IMPACC's SFDR performance when the central RF modulation frequencies are set to 23 GHz and 69.9 GHz, respectively. We note that the modulation linewidth around the central frequency 23 GHz is wider compared with case of central frequency of 69.9 GHz. On the other hand, in the non-resonance region, (defined as the region between the resonance regions), the SFDR is typically less than that obtained from the ideal MZI as shown

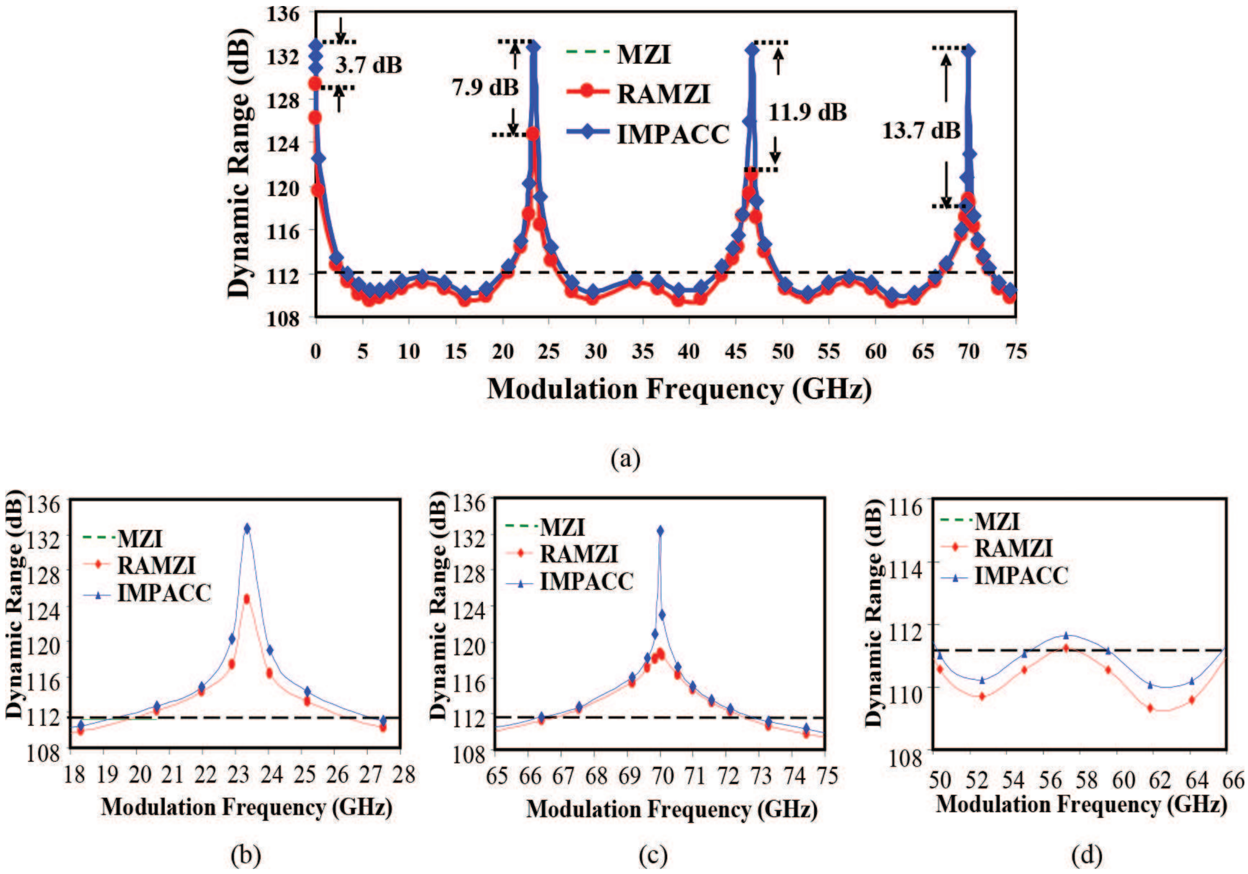

Figure 17. (a) Frequency response for the IMPACC, RAMZI, and MZI, (b) resonant region around a central modulation frequency of 23.3 GHz, (c) resonant region around a central modulation frequency of 70 GHz, (d) non-resonance region around 58 GHz. (analysis assumes a 1 Hz resolution bandwidth).

in **Figure 17(d)**. However, the IMPACC still shows an improved SFDR performance by 0.5 to 2.0 dB compared to RAMZI.

4.1.4.2. MRR lossy cases (OC, CC and UC Conditions)

Figure 18 depicts the SFDR performance of both IMPACC and RAMZI under over-coupled (OC), critical-coupled (CC), and under-coupled (UC) conditions. **Figure 18(a)** shows the OC IMPACC (τ = 0.6364, α = 0.7364) and OC RAMZI (τ = 0.2679, α = 1) as a function of the RF modulation frequency. As we have described earlier, in the regions close to the resonance peak (e.g., ~23 GHz), IMPACC clearly outperforms RAMZI, which operates under ideal condition by 10–20 dB.

The case of CC IMPACC is shown in **Figure 18(b)**. IMPACC also outperforms RAMZI within or in the resonant peak regions. Outside the resonant regions, both IMPACC and RAMZI have nearly the same performance. Lastly, **Figure 18(c)** shows IMPACC performance versus RAMZI in the case of UC condition at the same resonance region as above (e.g., modulation frequency ~23 GHz). In regions close to the resonance peak, the IMPACC still outperforms the ideal over-coupled RAMZI, but now the maximum difference is much smaller (e.g., ~4 dB). We note that

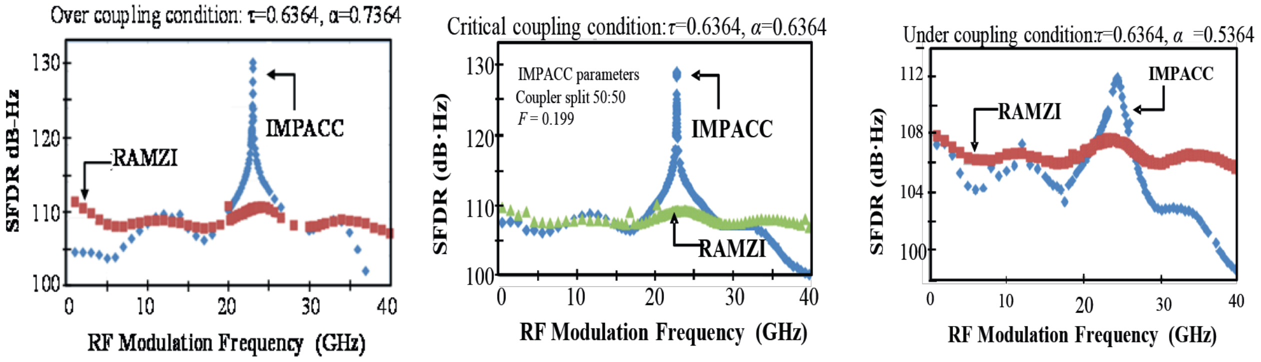

(a) (b) (c)

Figure 18. (a) SFDR comparison of IMPACC and RAMZI at (a) over-coupled condition, (b) critical-coupling condition, and (c) under-coupling condition for modulation frequency 23 GHz, $\xi_{PM} = 1.3893\pi$, $F = 0.2008$.

in all these situations, we did not optimize the performance of IMPACC by changing its external parameters (e.g., F or ξ_{PM}).

4.2. Adaptive operating mode of IMPACC

IMPACC's adaptive operating mode is all about using dynamically the two built-in, adjustable, and externally controllable two parameters to maintain IMPACC's 130 dB SFDR performance under unfavorable parameter conditions such as: (i) intrinsic RR loss, (ii) parameter variation of τ value, and (iii) unbalanced OS power split ratio. The unavoidable parameter variations can be due to (a) environmental temperature change, (b) device aging, and (c) fabrication tolerance and errors. The externally controllable parameters used for mitigation purposes are the RF power split ratio F, and the RF phase shift, ξ_{PM}. Here, we set the other RF phase shift, ξ_{MRR} equal to 0, for simplicity. Using again these two external parameters, we show that IMPACC can also extend its SFDR-vs-modulation bandwidth capability beyond that of RAMZI [91, 106–108, 110]. Overall, the adaptive mode of IMPACC allows the link design to be flexible with excellent results.

4.2.1. Extending parameter tolerance to ring resonator loss

The ability to adjust the control parameters F and ξ_{PM} can be exploited to compensate for the negative effect of loss factorα of MRR. In Section 4.1.1, we showed that the SFDR performance of both IMPACC and RAMZI can deteriorate by as much as ~20 dB when the RR loss factor (e.g., $\alpha < 1$) increases. This effect is reproduced in **Figure 19(a)** for IMPACC and RAMZI with fixed F values. **Figure 19(a)** also shows the SFDR performance for IMPACC with dynamic or adaptive F parameter value. The two cases with fixed F parameter value are similar to the one shown in **Figure 13(b)** and discussed in Section 4.1.1.

The result of this adaptive mode is to maintain the SFDR value to higher than 130 dB by dynamically changing the required F value as a function of the MRR loss factorα as shown in **Figure 19(b)**. It shows the range of required changes in the value of F to achieve the SFDR performance shown in **Figure 19(a)**. This unique ability of IMPACC overcomes the negative effect of the intrinsic insertion loss due to MRR. This feature is not feasible in RAMZI or any

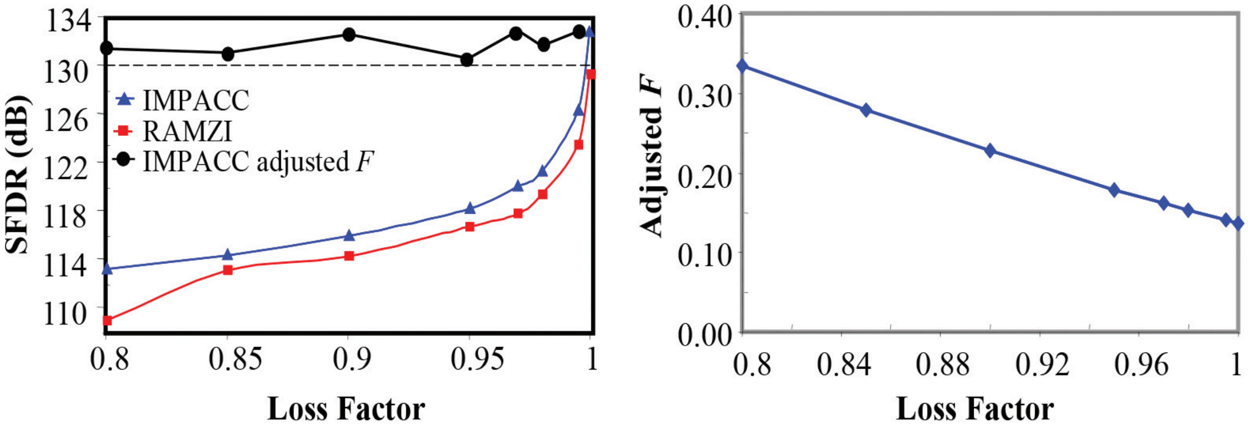

(a) (b)

Figure 19. (a) IMPACC compensates for MRR intrinsic losses to obtain SFDR values above 130 dB, (b) RF power split ratio adjustments required to achieve high SFDR (e.g., >130 dB) performance under MRR with exhibited insertion losses.

previously reported linear intensity modulators. It makes the link design and engineering more flexible.

4.2.2. Extending parameter tolerance to unbalanced split ratio of OS

4.2.2.1. Over-coupled (OC) IMPACC and critically-coupled (CC) IMPACC

In this section, we highlight IMPACC's ability to compensate the negative effect due to unbalanced optical splitter performance [110, 113]. **Figure 20(a)** shows the SFDR performance of OC IMPACC (τ = 0.6364, α = 0.7364) for unbalanced OS (55:45; green line), balanced (50:50; uncompensated; red line), and unbalanced (55:45; blue line) but compensated by adjusting the *F* parameter.

This is emphasized in **Figure 20(a)** where the original drop of 6 dB in the SFDR performance, when the optical splitter is nonideal (55:45), can be compensated to return to SFDR value equal to 129 dB by adjusting the external parameters, *F* and ξ_{PM} to 0.2003 and 1.307π, respectively.

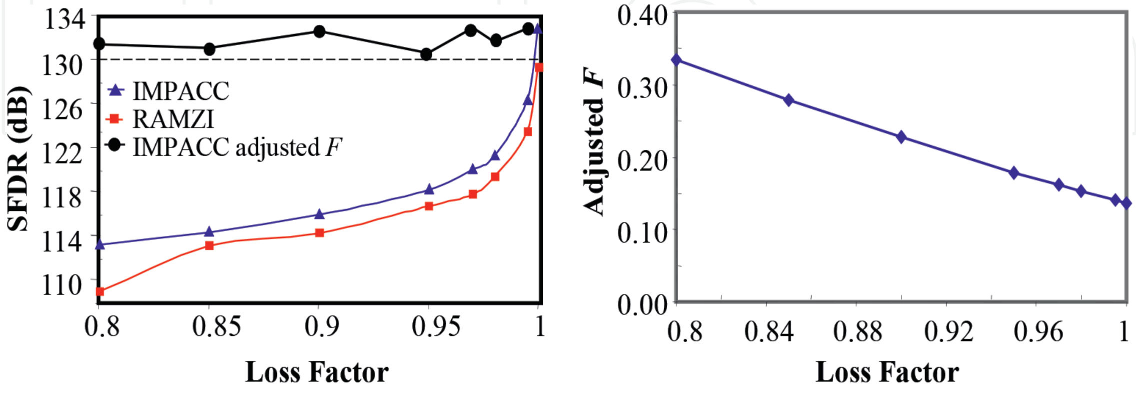

(a) (b)

Figure 20. SFDR comparison of (a) over-coupled and (b) critical-coupling condition for RAMZI and IMPACC for both unbalanced and balanced scenarios (modulation frequency 23 GHz, ξ_{PM} = 1.3893π, *F* = 0.2008).

Hence, clearly, IMPACC's inherent compensation capability is quite effective and able to overcome this limitation. **Figure 20(b)** depicts the SFDR performance of IMPACC at a power balanced for the case of CC condition (i.e., 50:50), unbalanced condition (e.g., 55:45) without compensation and with compensation for the case of CC condition. In the unbalanced condition, the SFDR drops 11 dB from 129 to 118 dB. Nevertheless, IMPACC's inherent compensation capability enables one to increase the SFDR back up to 129 dB for the unbalanced (55:45) case under CC by adjusting the F and ξ_{PM} parameters.

4.2.2.2. Under-coupled (UC) IMPACC

In UC condition, the inherent compensation capability of IMPACC is severely limited and cannot increase the SFDR of IMPACC for the unbalanced case. Adjusting the external parameters,F or ξ_{PM} do not improve the SFDR value. Similar to previous Section 4.1.3, we observed that the IMPACC SFDR performance (e.g., 111 dB) is still higher than that of RAMZI (e.g., 108 dB) but the difference is noticeably smaller compared with the over- and critical-coupled conditions with SFDR of around 129–130 dB.

4.2.3. Extending SFDR versus modulation bandwidth response

As discussed earlier in Section 4.1.3, all ring resonator based modulators (e.g., RAMZI and IMPACC) are limited by the FSR of the ring resonator [88, 91–92, 94,102,104–108]. This is graphically represented by the narrow Lorentzian shape of its SDFR profile as depicted in **Figures 17** and **18**. This limitation is troublesome, especially for wideband RF link applications. Fortunately, the IMPACC has significant advantage compared with RAMZI and other linear modulators that relaxes this built-in RF modulation bandwidth limitation due to MRR.

IMPACC can broaden the SFDR profile at its peak value by dynamically adjusting both F and ξ_{PM} for any given modulation frequency band. **Figure 21** shows this remarkable feature for a frequency of operation from 16 GHz to 20 GHz, where the IMPACC can maintain a SFDR of >130 dB. For the results presented in **Figure 21**, we have used λ = 1550 nm and τ = 0.208, and both the RF phase, ξ_{PM} and power split, F parameters were changed in other to maintain the

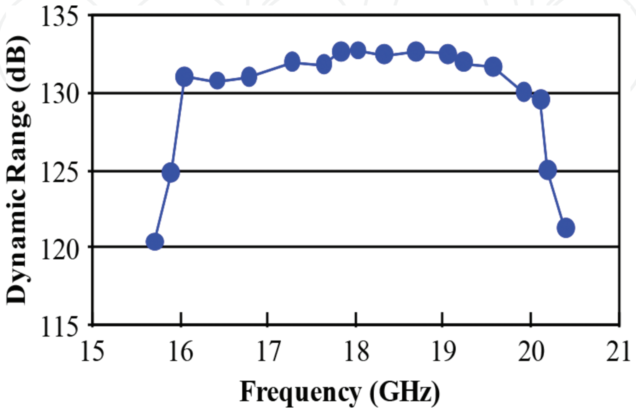

Figure 21. Changing the power split ratio F:(1−F) and RF bias, phase ξ_{PM}, of RF signal can achieve a flat SFDR response over a range of ~20% of around a central frequency (λ = 1550 nm).

high SFDR. We are not aware of any MRR-based modulator designs that can accomplish such a dynamically adjustable wide frequency response using externally controlled parameter.

5. Conclusion

In summary, electro-optic modulators are critical part of optical communications. They will continue to play an important role in fiber optic links. However, an essential requirement is that they have linear response with a high dynamic range of input RF powers of multiple tones. We have shown that IMPACC can operate with highly linear response with peak SFDR value of 132 dB.

Another important requirement in the link design is the inherent versatility of the device or link to compensate for unexpected changes or unavoidable parameter variations due to environmental temperature change, device aging, and fabrication errors. In this regard, IMPACC has a unique place among previously reported linear intensity modulators since it is the only linear modulator design, as far as we know, that has an inherent compensation capability. We demonstrated this inherent feature by compensating various nonideal and often detrimental effects in the modulator from RR waveguide loss and unbalanced optical inputs to various coupling conditions that could lower manufacturing tolerance and degrade linearity performance if not mitigated. The ability to maintain high SFDR (e.g., >130 dB) under these conditions makes IMPACC a viable candidate for many high-bandwidth RF FO-link applications, and well positioned as ideal linear intensity modulator for software-defined MPLs

Acknowledgements

NM would like to thank partial support from the European Committee under program FP7-MC-CIG 333829.

Author details

Benjamin Dingel[1,2]*, Nicholas Madamopoulos[3,4] and Andru Prescod[5]

*Address all correspondence to: bbdingel@stny.rr.com

1 Nasfine Photonics Inc., Painted Post, NY, USA

2 Ateneo Innovation Center, Ateneo De Manila University, Quezon City, Philippines

3 Department of Aeronautical Science, Hellenic Air Force Academy, Dekeleia, Greece

4 Department of Electrical Engineering, The City College of City University of New York, USA

5 ManTech International Corporation, Arlington, VA, USA

References

[1] Elbers J-P, Autenrieth A. From static to software-defined optical networks. In: 16th International Conference on Optical Network Design and Modeling (ONDM), 2012. IEEE; 2012

[2] Gringeri S, Bitar N, Xia TJ. Extending software defined network principles to include optical transport. IEEE Communications Magazine. 2013;**51**(3):32–40

[3] Amaya N, et al. Software defined networking (SDN) over space division multiplexing (SDM) optical networks: Features, benefits and experimental demonstration. Optics Express. 2014;**22**(3):3638–3647

[4] Chen X, Zhang Y. Intelligence on optical transport SDN. International Journal of Computer and Communication Engineering. 2015;**4**(1):5

[5] Kreutz D, et al. Software-defined networking: A comprehensive survey. Proceedings of the IEEE. 2015;**103**(1):14–76

[6] Thyagaturu AS, et al. Software defined optical networks (SDONs): A comprehensive survey. IEEE Communications Surveys & Tutorials. 2016;**18**(4):2738–2786

[7] Lannoo B. Radio-over-fibre for ultra-small 5G cells. In: 17th International Conference on Transparent Optical Networks (ICTON). 2015. pp. 1–4. DOI: 10.1109/ICTON.2015.7193591

[8] Waterhouse R, Novack D. Realizing 5G: Microwave photonics for 5G mobile wireless systems. IEEE Microwave Magazine. 2015;**16**(8):84–92

[9] Way WI. Broadband Hybrid Fiber/Coax Access System Technologies. San Diego, CA: Academic Press; 1998

[10] Al-Raweshidy H, Komaki S, editors. Radio over Fiber Technologies for Mobile Communications Networks. Norwood, MA: Artech House; 2002

[11] Llorente R, Beltrán M. Radio-over-fibre Techniques and Performance. Rijeka, Croatia: INTECH Open Access Publisher; 2010

[12] Liu C, et al. Key microwave-photonics technologies for next-generation cloud-based radio access networks. Journal of Lightwave Technology. 2014;**32**(20):3452–3460

[13] Ackerman E, Cox III C, Riza N, editors. Analog Fiber Optic Links. SPIE Milestone Series. Vol. MS-149; 1998

[14] Chang W, editor. RF Photonics Technologies in Optical Fiber Links. Cambridge, UK: Cambridge University Press; 2002

[15] Vilcot A, Cabon B, Chazelas J, editors. Microwave Photonics from Components to Applications. New York, NY: Kluwer Academic Publishers; 2003

[16] Cox III CH. Analog Optical Links: Theory and Practice. Cambridge, UK: Cambridge University Press; 2004

[17] Ji PN. Software defined optical network. In: 11th International Conference on Optical Communications and Networks (ICOCN), 2012. IEEE; 2012

[18] Channegowda M, et al. Experimental demonstration of an OpenFlow based software-defined optical network employing packet, fixed and flexible DWDM grid technologies on an international multi-domain test bed. Optics Express. 2013;**21**(5):5487–5498

[19] Simeonidou D, Nejabati R, Channegowda MP. Software defined optical networks technology and infrastructure: Enabling software-defined optical network operations. In: Optical Fiber Communication Conference and Exposition and the National Fiber Optic Engineers Conference (OFC/NFOEC); 2013. IEEE; 2013

[20] ONF Solution Brief. OpenFlow-enable Transport SDN. May 2014

[21] Capmany J, Novak D. Microwave photonics combines two worlds. Nature Photonics. 2007;**1**(6):319–330

[22] Marpaung D, et al. Integrated microwave photonics. Laser & Photonics Reviews. 2013;**7** (4):506–538

[23] Capmany J, Munoz P. Integrated microwave photonics for radio access networks. Journal of Lightwave Technology. 2014;**32**(16):2849–2861

[24] Guan B, et al. CMOS compatible reconfigurable silicon photonic lattice filters using cascaded unit cells for RF-photonic processing. IEEE Journal of Selected Topics in Quantum Electronics. 2014;**20**(4):359–368

[25] Iezekiel S, et al. RF engineering meets optoelectronics: Progress in integrated microwave photonics. IEEE Microwave Magazine. 2015;**16**(8):28–45

[26] Bowers JE. Integrated microwave photonics. In: 2015 International Topical Meeting on Microwave Photonics (MWP). IEEE; 2015

[27] Xu X, Bosisio RG, Wu K. Analysis and implementation of six-port software-defined radio receiver platform. IEEE Transactions on Microwave Theory and Techniques. 2006;**54**(7):2937–2943

[28] Ibrahim S, et al. Demonstration of a fast-reconfigurable silicon CMOS optical lattice filter. Optics Express. 2011;**19**(14):13245–13256

[29] Pérez D, Gasulla I, Capmany J. Software-defined reconfigurable microwave photonics processor. Optics Express. 2015;**23**(11):14640–14654

[30] Zhuang L, et al. Programmable photonic signal processor chip for radiofrequency applications. Optica. 2015;**2**(10):854–859

[31] Pérez D, et al. Reconfigurable lattice mesh designs for programmable photonic processors. Optics Express. 2016;**24**(11):12093–12106

[32] Wei W, et al. Software-defined microwave photonic filter with high reconfigurable resolution. Scientific Reports. 2016;**6**

[33] Capmany J, Gasulla I, Pérez D. Microwave photonics: The programmable processor. Nature Photonics. 2016;**10**(1):6–8

[34] Khan MH, et al. Ultrabroad-bandwidth arbitrary radiofrequency waveform generation with a silicon photonic chip-based spectral shaper. Nature Photonics. 2010;**4**(2): 117–122

[35] Burla M, et al. Integrated waveguide Bragg gratings for microwave photonics signal processing. Optics Express. 2013;**21**(21):25120–25147

[36] Pant R, et al. On-chip stimulated Brillouin scattering for microwave signal processing and generation. Laser & Photonics Reviews. 2014;**8**(5):653–666

[37] Shin H, et al. Control of coherent information via on-chip photonic–phononic emitter–receivers. Nature Communications. 2015;**6**. DOI: 10.1038/ncomms7472

[38] Wang J, et al. Reconfigurable radio-frequency arbitrary waveforms synthesized in a silicon photonic chip. Nature Communications 2015;**6**. DOI:10.1038/ncomms6957

[39] Liu W, et al. A fully reconfigurable photonic integrated signal processor. Nature Photonics. 2016;**10**(3):190–195

[40] Wang J, Long Y. A Chip-Scale Microwave Photonic Signal Processing. Rijeka, Croatia: INTECH Open Access Publisher; 2017

[41] Cox CH, et al. Limits on the performance of RF-over-fiber links and their impact on device design. IEEE Transactions on Microwave Theory and Techniques. 2006;**54**(2): 906–920

[42] Iezekiel S, editor. Microwave Photonics: Devices and Applications. Chichester, West Sussex, UK: John Wiley & Sons, Ltd; 2009

[43] Urick Jr VJ, Mckinney JD, Williams KJ. Fundamentals of microwave photonics. In: Chang K, editor. Wiley Series in Microwave and Optical Engineering. Hoboken, New Jersey: John Wiley & Sons, Inc.; 2015

[44] Urick VJ, Diehl JF, Draa MN, McKinney JD, Williams KJ. Wideband analog photonic links: Some performance limits and considerations for multi-octave implementations. In: Nelson RL, Prather DW, Schuetz C, editors. Proceedings of the SPIE, RF and Millimeter-Wave Photonics II; 2012. Vol. 8259:825904

[45] Bridges W, Shaffner J. Distortion in linearized electrooptic modulators. IEEE Transactions on Microwave Theory and Techniques. 1995;**43**(9):2184–2197. DOI: 10.1109/22.414563

[46] Ridder RM, Korotky S. Feedforward compensation of integrated optic modulator distortion. In Proceedings of the Technical Digest Optical Fiber Communications Conference, San Francisco, CA; 1990

[47] Chiu Y, et al. Broad-band electronic linearizer for externally modulated analog fiber-optic links. IEEE Photonics Technology Letters. 1999;**11**(1):48–50

[48] Sadhwani R, Basak J, Jalali B. Adaptive electronic linearization of fiber optic links. In: Optical Fiber Communication Conference. Optical Society of America; 2003

[49] Sadhwani R, Jalali B. Adaptive CMOS predistortion linearizer for fiber-optic links. Journal of Lightwave Technology. 2003;**21**(12):3180–3193

[50] Killey RI, et al. Electronic dispersion compensation by signal predistortion using digital processing and a dual-drive Mach-Zehnder modulator. IEEE Photonics Technology Letters. 2005;**17**(3):714–716

[51] Säckinger E. Broadband Circuits for Optical Fiber Communication. John Wiley & Sons; 2005

[52] Moon H, Sedaghat R. FPGA-based adaptive digital predistortion for radio-over-fiber links. Microprocessors and Microsystems. 2006;**30**(3):145–154

[53] Lee T-K, et al. Theoretical analysis and realization of optoelectrical predistortion optical transmitter for the simultaneous suppression of IM3 and IM5 signal. Optics Communications. 2012;**285**(10):2697–2701

[54] Lam D, et al. Digital broadband linearization of optical links. Optics Letters. 2013;**38**(4):446–448

[55] Schmidta C, Kottkea C, Jungnickela V, Freunda R. High-speed digital-to-analog converter concepts. In: Proceedings of the SPIE; 2017, January, Vol. 10130, pp. 101300N-1

[56] Lee G-W, Han S-K. Linear dual electroabsorption modulator for analog optical transmission. Microwave and Optical Technology Letters. 1999;**22**(6):369–373

[57] Betts GE, et al Gain limit in analog links using electroabsorption modulators. IEEE Photonics Technology Letters. 2006;**18**(19):2065–2067

[58] Xie XB, et al. Analysis of linearity of highly saturated electroabsorption modulator link due to photocurrent feedback effect. Optics Express. 2007;**15**(14):8713–8718

[59] Kogelnik H, Schmidt RV. Switched directional couplers with alternating Δβ. IEEE Journal of Quantum Electronics. 1976;**12**:396–401

[60] Thaniyavarn S. Modified 1×2 directional coupler waveguide modulator. Electronics Letters. 1986;**22**:941–942

[61] Tavlykaev RF, Ramaswamy RV. Highly linear Y-fed directional coupler modulator with low intermodulation distortion. Journal of Lightwave Technology. 1999;**17**:282–291

[62] Zhang X, et al. Highly linear broadband optical modulator based on electro-optic polymer. IEEE Photonics Journal. 2012;**4**(6):2214–2228

[63] Li J, et al. Optical sideband processing approach for highly linear phase-modulation/direct-detection microwave photonics link. IEEE Photonics Journal. 2014;**6**(5):1–10

[64] Zheng X-P, et al. All-optical signal processing for linearity enhancement of Mach–Zehnder modulators. Chinese Science Bulletin. 2014;**59**(22):2655–2660

[65] Chen J, Zhu D, Pan S. Linearized phase-modulated analog photonic link based on optical carrier band processing. In: 25th Wireless and Optical Communication Conference (WOCC); 2016. IEEE; 2016

[66] Tazawa H, Steier W. Linearity of ring resonator-based electro-optic polymer modulator. Electronics Letters. 2005;**41**(23):1297–1298

[67] Tazawa H, Steier WH. Analysis of ring resonator-based traveling-wave modulators. IEEE Photonics Technology Letters. 2006;**18**(1):211–213

[68] Song M, Zhang L, Beausoleil RG, Willner AE. Nonlinear distortion in a silicon microring-based electro-optic modulator for analog optical links. IEEE Journal of Selected Topics in Quantum Electronics. 2010;**16**(1):185–191

[69] Fegadolli W, Oliveira JEB, Almeida VR. Highly linear electro-optic modulator based on ring resonator. Microwave Optics Technology Letters. 2011;**53**(10):2375–2378

[70] Ayazi A, Baehr-Jones T, Liu Y, Lim AE-J, Hochberg M. Linearity of silicon ring modulators for analog optical links. Optics Express. 2012;**20**(12):13115–13122

[71] Chen L, Chen J, Nagy J, Reano RM. Highly linear ring modulator from hybrid silicon and lithium niobate. Optics Express. 2015;**23**(10):13255–13264

[72] Hosseinzadeh A, Middlebrook CT. Highly linear dual ring resonator modulator for wide bandwidth microwave photonic links. Optics Express. 2016;**24**(24):27268–2727924

[73] Yariv A, Yeh P. Optical Waves in Crystals-Propagation and Control of Laser radiation. New York, NY: John Wiley and Sons; 1984

[74] Johnson LM, Roussell HV. Reduction of intermodulation distortion in interferometric optical modulators. Optics Letters. 1988;**13**(10):928–930

[75] Johnson LM, Roussell HV. Linearization of an interferometric modulator at microwave frequencies by polarization mixing. IEEE Photo Technology Letters. 1990;**2**(11):810–811

[76] Djupsjobacka A. A linearization concept for integrated-optic modulators. Photonics Technology Letters. 1992;**4**(8):869–871

[77] Ho KP, Kahn JM. Optical frequency comb generator using phase modulation in amplified circulating loop. IEEE Photonics Technology Letters. 1993;**5**(6):721–725

[78] Betts GE, O'Donnell FJ. Optical analog link using a linearized modulator. In: IEEE LEOS Annual Meeting, 31 Oct.–3 Nov. 1994; Vol. 2, pp. 278–279

[79] Betts GE. Linearized modulator for suboctave-bandpass optical analog links. IEEE Transactions Microwave Theory Technology. 1994;**42**(12):2642–2649

[80] Sabido DJM, Tabara M, Fong TK, Lu CL, Kazovsky LG. Improving the dynamic range of a coherent AM analog optical link using a cascaded linearized modulator. IEEE Photonics Technology Letters. 1995; **7**(7):813–815

[81] Burns WK. Linearized optical modulator with fifth order correction. IEEE Journal of Lightwave Technology. 1995;**13**(8):1724–1727

[82] Betts GE, O'Donnell FJ. Microwave analog optical links using suboctave linearized modulators. Photonics Technology Letters. 1996;**9**(8):1273–1275

[83] Loayssa A, Alonso M, Benito D, Garde MJ. Linearization of electro-optic modulators at millimeter-wave frequencies. In: Proceedings of the LEOS '99 - 12th Annual Meeting. 8–11 November 1999; Vol. 1, pp. 275–276

[84] Ackerman EI. Broad-band linearization of a Mach-Zehnder electro-optic modulator. IEEE Transactions on Microwave Theory and Techniques. 1999;**47**(12):2271–2279

[85] Yariv A. Universal relations for coupling of optical power between microresonators and dielectric waveguides. Electronics Letters. 2000;**36**:321–322

[86] Okamoto K. Fundamentals of Optical Waveguides. Burlington, MA: Academic Press; 2000

[87] Rengand N, Shpantzer I, Achiam Y, Kaplan A, Greenbalatt A, Harston G, Cho PS. Military Communications Conference. IEEE MILCOM 2003. 13–16 Oct. 2003;2:1208

[88] Xie X, Khurgin J, Kang J, Chow FS. Linearized Mach-Zehnder intensity modulator. IEEE Photonics Technology Letters 2003;**15**(4):531–533

[89] Dingel B. Ultra-linear, broadband optical modulator for high performance analog fiber link system. In: IEEE International Topical Meeting on Microwave Photonics 2004 (MWP'04); 4–6 Oct. 2004. pp. 241–244

[90] Schwelb O. Transmission, group delay, and dispersion in single-ring optical resonators and add/drop filters – A tutorial overview. Journal of Lightwave Technology. 2004;**22**: 1380–1394

[91] Tazawa H. Ring resonator based electro-optic polymer modulators for microwave photonics applications [Ph.D. thesis]. Los Angeles, CA: University Southern California; 2005

[92] Tazawa H, Steier W. Bandwidth of linearized ring resonator assisted Mach-Zehnder modulator. IEEE Photonics Technology Letters. 2005;**17**(9):1851–1853

[93] Dingel B. Linear optical modulator. US Patent 6943931, Sept. 2005

[94] Dingel BB, Madabhushi R, Madamopoulos N. Super-linear optical modulator technologies for optical broadband access network: Development and potential. In: SPIE Proceeding 6012, Optical Transmission Systems and Equipment for WDM Networking IV, October 2005; paper No. 32, Boston

[95] Chen WY, Van V, Herman WN, Ho PT. Periodic microring lattice as a bandstop filter. IEEE Photonics Technology Letters. 2006;**18**(19):2041–2043

[96] Madamopoulos N, Dingel B. Performance analysis of the ultra-linear optical intensity modulator. In: Proceedings of the SPIE 6390, Optical Transmission Systems and Equipment for Networking V, October 2006; paper No. 15, Boston

[97] Van V, Herman W, Ho PT. Linearized microring-loaded mach-zehnder modulator with RF gain. IEEE Journal of Lightwave Technology. 2006;**24**(4):1850–1854

[98] Tazawa H, Kuo YH, Dunayevskiy I, Luo J, Jen A, Fetterman H, Steier W. Ring resonator-based electrooptic polymer traveling-wave modulator. IEEE Journal of Lightwave Technology. 2006;**24**(9):3514–3519

[99] Oliveira JEB, Sakamoto BFR, dos Santos Fegadolli W. Similarities between birefringent gires tournois interferometer and double ring assisted Mach Zehnder. In: European Microwave Conference, Munich; 9–12 Oct 2007. pp. 1330–1333

[100] Zhu G, Liu W, Fetterman HR. A broadband linearized coherent analog fiber-optic link employing dual parallel Mach–Zehnder modulators. IEEE Photonics Technology Letters. 2009:**21**(21):1627–1629

[101] Prescod A, Dingel B, Madamopoulos N. Super-linear modulator with extended bandwidth capability for broadband access applications. In: Proceedings of the SPIE OPTO 2009, Vol. 7234, San Jose, CA; Jan. 24–29, 2009

[102] Prescod A, Dingel BB, Madamopoulos N. Traveling wave optical modulator with high dynamic range (<<130 dB) at large modulation frequencies. In: Proceedings 2009 IEEE Sarnoff Symposium, Session: Optical Communications and Networking, Princeton, NJ; March 30–April 1, 2009. pp. 1–5

[103] Prescod A, Dingel B, Madamopoulos N. An ultra-linear modulator with inherent SFDR compensation capability. In Proceedings of the OSA Integrated Photonics Research, Silicon and Nano Photonics (IPR), July 27, 2010, Monterey, California, USA

[104] Prescod A, Dingel BB, Madamopoulos N, Madabhushi R. Effect of ring resonator waveguide loss on SFDR performance of highly linear optical modulators under suboctave operation. Photonics Technology Letters. 2010;**22**(17):1297–1299

[105] Dingel B, Prescod A, Madamopoulos N. Inherent RF linearized bandwidth broadening capability of an ultra-linear optical modulator. In: Proceedings of the SPIE 7958, Broadband Access Communication Technologies IV; January 2011; paper 7958–3, San Francisco, CA

[106] Dingel B, Madamopoulos N, Prescod A, Madabhushi R. Analytical model, analysis and parameter optimization of a super linear electro-optic modulator (SFDR > 130 dB). Optics Communications. 2011;**284**(24):5578–5587

[107] Madamopoulos N, Dingel B, Prescod A. Interferometric modulator with phase-modulating and cavity-modulating components (IMPACC) for high linearity microwave applications. In Proceedings of the ICPS 2013, The International Conference on Photonics Solutions, Pattaya City, Thailand, May 26–28, 2013 (Co-sponsored by OSA, SPIE, IEEE)

[108] Madamopoulos N, Dingel BB, Prescod A. Review and challenges of high frequency cavity-assisted electro-optic modulators. In: Wireless Optical Communication Conference, WOCC 2014, Newark, NJ, USA; 2014

[109] Jiang W, et al. A linearization analog photonic link with high third-order intermodulation distortion suppression based on dual-parallel Mach–Zehnder modulator. IEEE Photonics Journal. 2015;**7**(3):1–8

[110] Dingel B, Madamopoulos N, Prescod A, Madabhushi R. Power balancing effect on the performance of IMPACC modulator under critical coupling (CC), over coupling (OC), and under coupling (UC) conditions at high frequency. Proceedings of the SPIE Broadband Access Communication Technologies. 2012;**VI**:828208

[111] Ye B, Dingel BB, Cui W. Minimalist-design, high-functionality, micro-ring resonator-based optical filter with narrow linewidth and low group delay using Looped Back Over- and Under-coupled Resonator (LOBOUR). Proceedings of the SPIE. Broadband Access Communication Technologies VII. 2013;8645:86450T

[112] Dingel B, Ye B, Cui W, Madamopoulos N. High-performance, minimalist-design, microring resonator-based optical filter with reduced low group delay and simplified center-wavelength control. International Conference on Photonics Solutions 2013. Thailand; 2013

[113] Dingel B, Prescod A, Madamopoulos N, Madabhushi R. Performance of ring resonator-based linear optical modulator (IMPACC) under critical coupling (CC), over coupling (OC), and under coupling (UC) conditions. In: IEEE Photonics Annual Society Meeting; 2011